Hierarchical Bayesian Physics-Informed Network Model for Open-Hole Wellbore Instability: From Parameter Uncertainty to Reliability Assessment

Zehua Song[a], Yu Song[a,*], Jin Yang[b], Kejin Chen[b], Jianqiao Zhang[c], Xing Wang[d]

[a]College of Artificial Intelligence, China University of Petroleum (Beijing), Beijing, 102249, China
[b]College of Safety and Ocean Engineering, China University of Petroleum (Beijing), Beijing, 102249, China
[c]School of Energy and Resources, Nanjing University, Suzhou, 215163, China
[d]College of Petroleum Engineering, China University of Petroleum (Beijing), Beijing, 102249, China

Abstract

This study addresses open-hole wellbore instability under coupled seepage, stress, thermal, and hydration effects. High-fidelity, multiphysics governing equations were formulated to capture the nonlinear stability evolution of the surrounding rock. A 2D numerical model was developed in COMSOL Multiphysics, and multi-parameter simulations were performed to generate a high-dimensional dataset characterizing the evolution of Von Mises stress, plastic strain, pore pressure, temperature, and water content. The model was validated for physical correctness and numerical stability. Furthermore, a hierarchical Bayesian physics-informed network (HBPINN) is proposed, integrating governing equation residuals with boundary conditions. Using Bayesian inference, this framework performs posterior estimation of key formation parameters and predicts the failure probability field. Training results show the HBPINN outperforms traditional neural networks in spatio-temporal extrapolation, physical consistency, and risk prediction. A case study was conducted on an open-hole well in China's Bohai Sea. Using mechanical parameters from compression tests, the earliest failure time profile was inferred, identifying high-risk zones predicted to fail in as little as 100 hours. This research provides a novel algorithmic framework for multiphysics-based instability prediction and dynamic reliability assessment of open-hole wellbores.

Keywords: Open-hole wellbore stability, Multiphysics coupling, Physics-informed neural network, Uncertainty quantification, Instability risk prediction

1. Introduction

Driven by the global energy transition and carbon-neutrality strategies, the development of offshore oil and gas fields has become crucial for improving economic efficiency Dongo and Relvas (2025); Zhou (2023). This is especially true for wells with long open-hole sections and significant bedding anisotropy. The coupled effects of hydration, stress, and temperature, induced by the dynamic seepage of drilling fluid, significantly increase the risk of progressive wellbore instability Siddiqui et al. (2024); Ma et al. (2025). Statistics show that in the Bohai Sea and surrounding waters, improper casing deployment timing accounts for 23% of non-productive time, with the cost of a single incident potentially exceeding 20 million USD Krygier et al. (2020). These challenges demand an intelligent warning system to predict the stability evolution of open-hole sections in real-time and with high accuracy Song et al. (2025); Fan et al. (2025). Additionally, it should support critical decisions on casing-setting time to ensure continuous, safe, and economic drilling operations Kamgue Lenwoue et al. (2023).

Traditional wellbore stability assessment has primarily relied on the static safety factor method, which is based on elasto-plastic finite element methods and the Mohr–Coulomb criterion. This method is also included in the API RP 13B-1 standard Institute, AP (2017). However, such methods neglect the time-dependent pore pressure evolution caused by dynamic drilling fluid seepage. Consequently, their prediction accuracy is limited and often biased in formations with pronounced bedding or strong heterogeneity. Recent innovative approaches still face key technical bottlenecks. In the domain of high-fidelity numerical simulation, Pirhadi et al. developed a coupled thermo-poro-elastic finite element model that demonstrated how drilling fluid temperature affects tensile and shear failure modes in depleted reservoirs Pirhadi et al. (2023). However, their model did not consider the additional effect of mechanical weakening due to hydration, making it less suitable for shale formations. Ding et al. established a coupled stress-unloading and hydration model to quantify the damage mechanism from bedding weakening and fluid invasion, but their analysis did not incorporate the time-dependent shielding effect of mud cake deposition Ding et al. (2023). Saber et al. used a COMSOL dual-porosity model to optimize horizontal well trajectories, but the model's heavy reliance on reservoir-specific inversion parameters limited its generalizability Saber et al. (2024). Feng et al. proposed a method for simulating dynamic mud cake thickness and permeability evolution Feng et al. (2018). However, their model simplified the stress-

*Corresponding author.
Email address: songyu_cup@163.com (Yu Song)

dependent evolution of the mud cake and did not fully couple the entire seepage–stress feedback mechanism, leading to inaccurate predictions for long-term exposure.

In the field of data-driven surrogate modeling, spurred by the success of deep learning in related geological tasks like lithology recognition Zhang et al. (2024a); Li et al. (2025), Wu et al. used artificial neural networks (ANNs) to predict open-hole stability based on data from adjacent wells, thereby reducing empirical subjectivity Wu et al. (2024a). However, this approach is limited by its training data domain and performs poorly in new exploration areas. Udegbunam et al. quantified the impact of input parameter uncertainty on collapse pressure using Monte Carlo methods but ignored the strong correlations between formation parameters and error accumulation effects Udegbunam et al. (2014). Chen et al. introduced the Nataf transform and Kolmogorov–Smirnov test to build a risk analysis framework for non-independent parameters, significantly reducing the prediction uncertainty Chen et al. (2024). However, the increased model complexity hindered its potential for real-time applications. Rafieepour et al. proposed a simplified chemo-thermo-poro-elastic model to enhance engineering usability Rafieepour et al. (2020); however, the exclusion of an anisotropic damage mechanism resulted in an inadequate response to early-stage instability processes, a common challenge when modeling rock failure in complex formations Zhang et al. (2024b).

Meanwhile, methods for dynamic drilling risk assessment have also gained significant attention Liu et al. (2022); Wu et al. (2023, 2024b). However, they generally suffer from two major limitations. While high-fidelity multiphysics models detail the instability mechanism, their large computational load prevents real-time, minute-level application. While high-fidelity multiphysics models detail the instability mechanism, their large computational load prevents real-time, minute-level application. Conversely, data-driven methods are fast but lack physical constraints, undermining their reliability when extrapolated to complex well sections. Against this backdrop, an intelligent modeling system that integrates physical mechanism modeling with uncertainty quantification offers significant development potential Jerez et al. (2024); Wang et al. (2024); Song et al. (2024); He et al. (2025). The core scientific challenge lies in building a hybrid intelligent framework that can simultaneously integrate the mechanisms of hydration diffusion, pore pressure evolution, thermal stress accumulation, and plastic damage, while also balancing inference efficiency, prediction accuracy, and model generalization.

To address the need for simulating and predicting instability under multiphysics disturbances, this study develops a hierarchical Bayesian physics-informed network (HBPINN) modeling framework. Based on physics-informed neural networks (PINNs), this method introduces a multi-branch network structure that systematically constrains neural network outputs with physical laws, using residuals from the Darcy flow, heat diffusion, hydration diffusion, and Drucker–Prager yield criterion equations, combined with initial and boundary condition errors. Furthermore, the framework integrates a two-stage Bayesian inference module for uncertainty quantification. First, prior distributions are assigned to key formation parameters, such as the initial elastic modulus and cohesion, and an approximate likelihood function is constructed based on the HBPINN's predictions and the physical residuals. Posterior inference of these parameters is then performed using Markov Chain Monte Carlo (MCMC) methods. Second, based on the obtained posterior parameter samples and a constructed engineering failure criterion based on a dual stress–strain judgment, uncertainty propagation analysis is carried out to infer the dynamic failure probability field, reliability evolution curve, and safe exposure time window. These results provide a quantitative basis for decision-making on casing setting times in open-hole sections.

2. Workflow

High-Fidelity Simulation of Coupled Seepage–Stress–Thermal–Hydration Wellbore State: A high-fidelity numerical model is developed in a 2D plane strain, polar coordinate system. This model simulates the stability response of the open-hole section during exposure. The model combines the Biot momentum conservation equation, Darcy's seepage equation, the heat transfer equation, and the hydration diffusion equation. Additionally, it incorporates hydration-dependent rock strength degradation relationships and a state-dependent Drucker–Prager yield criterion. This approach systematically captures the nonlinear deformation behavior under multiphysics disturbances. Parameter inputs are based on logging and core sample statistics from the Caofeidian block. A stratified Latin Hypercube sampling strategy is employed to generate a global sample set that covers variations in lithology, permeability, and thermal and hydration properties. Adaptive mesh refinement ensures computational accuracy in high-gradient regions near the wellbore wall. The final outputs include spatio-temporal evolution sequences of the equivalent stress field, plastic strain field, pore pressure, and water content. These results provide high-quality samples and strong physical constraints for subsequent PINN modeling.

HBPINN Construction and Training: The HBPINN builds on the PINN framework for efficient inference and uncertainty characterization of the wellbore's state evolution under multiphysics disturbances. The network architecture consists of a physics-driven multi-branch network and a Bayesian inference module. The former uses a deep feedforward neural network to predict multiphysics variables and is trained with governing equation residuals as constraints. The latter achieves uncertainty modeling through a two-stage process of parameter inference and risk quantification. First, an approximate likelihood function is constructed based on the network predictions, and the posterior distribution of key rock parameters is inferred using MCMC methods. Second, this posterior distribution and an engineering failure criterion are used to perform uncertainty propagation analysis, quantifying the failure probability and reliability of the wellbore. The overall loss function combines PDE residuals, initial and boundary condition errors, and limited observation data terms. The network uses adaptive weights to balance data-driven aspects with physical consistency, enabling high-reliability inference under high uncertainty. The workflow is illustrated in Fig. 1.

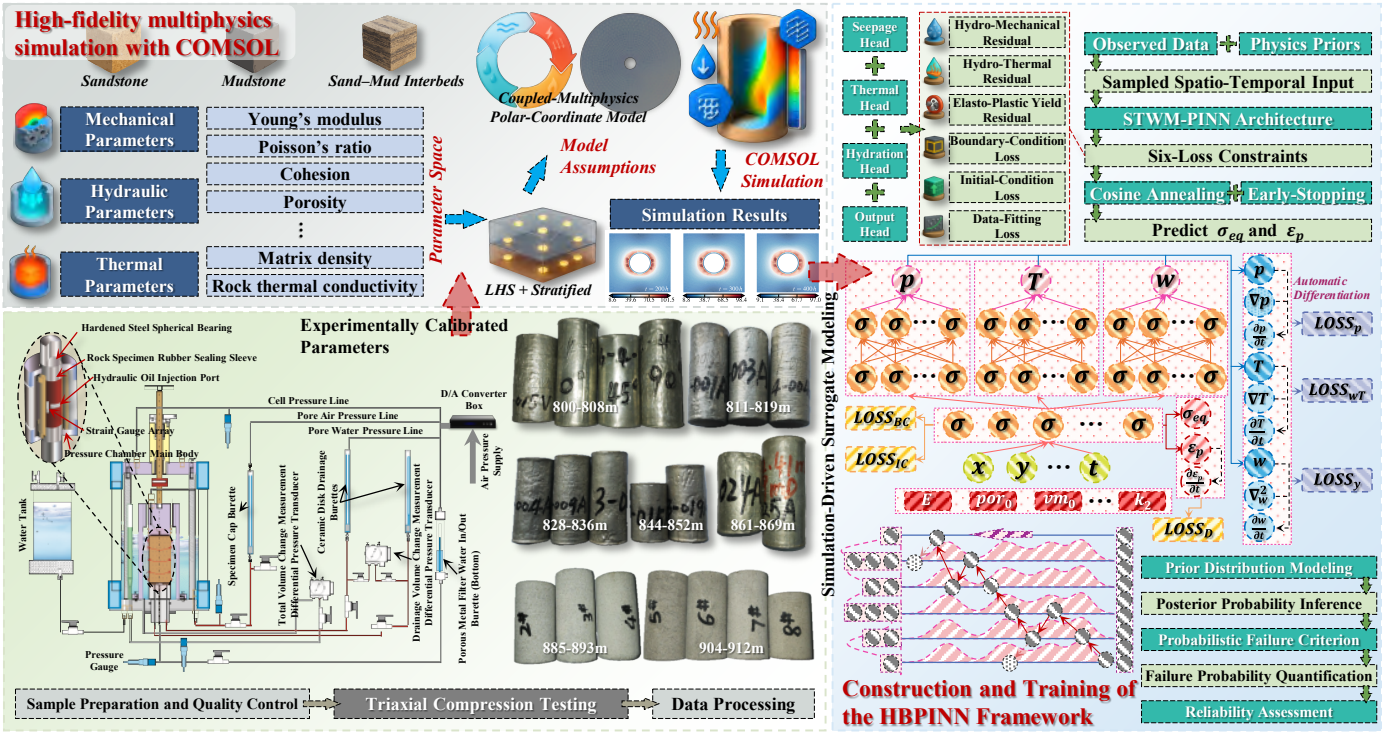


Figure 1: Workflow of HBPINN.

3. Multiphysics Coupled Model Simulation

3.1. Coupled Governing Equations

This study addresses the instability of open-hole wellbores induced by coupled seepage, stress, thermal, and hydration effects in complex formations. A set of high-fidelity, multiphysics governing equations was established, integrating seepage disturbance, hydration softening, temperature diffusion, and elasto-plastic response. The coupled model captures the nonlinear stability evolution of the rock mass under drilling fluid invasion, heat exchange, and lithological changes. This provides a unified theoretical baseline for high-fidelity simulation and physics-constrained learning.

For the mechanical control, the stress equilibrium in a consolidated porous medium is governed by the modified Biot momentum conservation equation Biot (1941):

$$\sigma_{ij,j} - (\alpha\delta_{ij}p)_{,j} + f_i = 0 \tag{1}$$

where σ_{ij} is the effective stress tensor (MPa), p is the pore pressure (MPa), α is the Biot coefficient (dimensionless), δ_{ij} is the Kronecker delta (dimensionless), and f_i is the body force vector (MPa).

The local strain response of the rock mass satisfies the incremental elasto-plastic constitutive relationship Lubliner (2008):

$$\begin{cases} d\varepsilon_{ij} = d\varepsilon^e_{ij} + d\varepsilon^p_{ij} + d\varepsilon^T_{ij} + d\varepsilon^w_{ij} \\ d\sigma_{ij} = [D_e]d\varepsilon^e_{ij} \end{cases} \tag{2}$$

where $d\varepsilon_{ij}$ is the total strain increment (dimensionless); $d\varepsilon^e_{ij}$, $d\varepsilon^p_{ij}$, $d\varepsilon^T_{ij}$, and $d\varepsilon^w_{ij}$ are the elastic, plastic, thermal expansion, and hydration expansion strain increments, respectively; $d\sigma_{ij}$ is the effective stress increment (MPa); and $[D_e]$ is the elastic stiffness matrix (MPa).

The plastic strain increment follows the associated flow rule Lubliner (2008):

$$d\varepsilon^p_{ij} = d\lambda\frac{\partial g}{\partial\sigma_{ij}} \tag{3}$$

where g is the plastic potential function (MPa) and $d\lambda$ is the plastic multiplier increment (dimensionless). Under ideal plastic conditions, $g = F$, where F is the yield function.

The Drucker–Prager criterion is adopted as the yield criterion, which is suitable for failure analysis in mixed sand-shale formations Drucker and Prager (1952):

$$F(I_1, J_2) = aI_1 + \sqrt{J_2} - k \tag{4}$$

where F is the yield function (MPa); a and k are material parameters related to the rock's cohesion c and internal friction angle ϕ (the conversion is defined by Eq. (17)); I_1 is the first stress invariant (MPa); and J_2 is the second deviatoric stress invariant (MPa²). They are calculated as follows:

$$\begin{cases} I_1 = \sigma_1 + \sigma_2 + \sigma_3 \\ J_2 = 1/6[(\sigma_1 - \sigma_2)^2 + (\sigma_2 - \sigma_3)^2 + (\sigma_3 - \sigma_1)^2] \end{cases} \tag{5}$$

where $\sigma_1, \sigma_2, \sigma_3$ are the principal effective stresses (MPa).

The volumetric expansion strain increments caused by hydration and thermal effects are defined as Coussy (2004):

$$\begin{cases} d\varepsilon^w_{ij} = \delta_{ij}[k_1 dw + k_2(dw)^2] \\ d\varepsilon^T_{ij} = \delta_{ij}[\alpha_T dT] \end{cases} \tag{6}$$

where dw is the water content increment (dimensionless); dT is the temperature increment (°C); k_1 and k_2 are hydration expansion coefficients; and α_T is the thermal expansion coefficient (1/°C).

Mechanical degradation due to hydration is described by the following water-content-dependent evolution relationships Huang et al. (2014):

$$\begin{cases} E = E_0 \cdot e^{-11\sqrt{(w-w_0)}} \\ v = 0.2 + 1.3w \\ c = c_0 - 250(w - w_0) \\ \phi = \phi_0 - 187.5(w - w_0) \end{cases} \tag{7}$$

where E is the elastic modulus (MPa); E_0 is the initial elastic modulus (MPa); v is the Poisson's ratio (dimensionless); c is the cohesion (MPa); c_0 is the initial cohesion (MPa); ϕ is the internal friction angle (°); ϕ_0 is the initial internal friction angle (°); w is the current water content (dimensionless); and w_0 is the initial water content (dimensionless).

The spatio-temporal distribution of water content w around the wellbore is governed by a 2D heat-conduction-like diffusion equation Biot (1941):

$$\begin{cases} \partial w/\partial t = D\left(\partial^2 w/\partial x^2 + \partial^2 w/\partial y^2\right) \\ w|_{r=r_w} = w_s \\ w|_{r\to\infty} = w_0 \end{cases} \tag{8}$$

where D is the hydration diffusion coefficient (m²/s); w_s is the saturated water content at the wellbore wall (dimensionless); r is the radial coordinate (m); and r_w is the wellbore radius (m).

The pore pressure p is governed by a 2D seepage equation based on Darcy's law and mass conservation Coussy (2004):

$$\frac{\partial}{\partial x}\left(\frac{\rho_w k}{\mu_0}\frac{\partial p}{\partial x}\right) + \frac{\partial}{\partial y}\left(\frac{\rho_w k}{\mu_0}\frac{\partial p}{\partial y}\right) + \phi\rho_w\gamma_l\frac{\partial p}{\partial t} + \rho_w\frac{\partial \phi}{\partial t} = 0 \tag{9}$$

where ρ_w is the filtrate density (kg/m³); k is the formation permeability (m²); μ_0 is the filtrate dynamic viscosity (Pa·s); ϕ is the porosity (dimensionless); γ_l is the liquid compressibility (1/MPa); and t is time (s).

Considering the porosity evolution caused by skeleton deformation, the relationship between porosity and volumetric strain is Coussy (2004):

$$\begin{cases} \partial\phi/\partial t = (1 - \phi_0)/(1 + \varepsilon_v)^2 \cdot (\partial\varepsilon_v/\partial t) \\ \varepsilon_v = \varepsilon_x + \varepsilon_y \end{cases} \tag{10}$$

where ε_v is the volumetric strain (dimensionless); ϕ_0 is the initial porosity (dimensionless); and ε_x, ε_y are the principal strain components (dimensionless).

Thermal coupling is described by the heat transfer equation for porous media Nield and Bejan (2006):

$$\begin{cases} \lambda_{\text{eff}} = \phi\lambda_w + (1 - \phi)\lambda_s \\ (\phi\rho_w C_M + (1 - \phi)\rho_s C_s)\dfrac{\partial T}{\partial t} \\ \quad - (\rho_w C_M)\dfrac{k}{\mu_0}\nabla p \cdot \nabla T = \nabla \cdot (\lambda_{\text{eff}}\nabla T) \end{cases} \tag{11}$$

where T is the temperature (°C); C_M is the filtrate specific heat (J/(kg·K)); λ_s is the rock thermal conductivity (W/(m·K)); λ_{eff} is the effective thermal conductivity of the porous medium (W/(m·K)); λ_w is the fluid thermal conductivity (W/(m·K)); ρ_s is the rock matrix density (kg/m³); and C_s is the rock skeleton specific heat (J/(kg·K)).

3.2. Model Assumptions and Boundary Conditions

A high-fidelity COMSOL Multiphysics model was constructed to accurately characterize the wellbore state evolution. The model was developed based on 2D plane strain theory in a polar coordinate system centered on the wellbore. The simulation domain was significantly larger than the wellbore diameter to minimize far-field boundary effects. The wellbore cross-section was assumed to be circular. Within a local structural unit, the formation was treated as a homogeneous and isotropic porous elastic material, satisfying the prerequisites of continuum mechanics.

Boundary and initial conditions were defined following the rock's physical evolution mechanisms. For the mechanical boundary, a uniform radial pressure equivalent to the drilling fluid column was applied to the wellbore wall to simulate its support effect. The far-field boundary was loaded with the regional maximum and minimum horizontal principal stresses to reproduce the influence of the in-situ stress field on the near-wellbore stress concentration. For the seepage field, the wellbore was set as a first-type boundary condition with a constant pore pressure determined by the drilling fluid, acting as a stable source for filtrate invasion. The far-field was set as a second-type boundary condition with a zero-pore pressure gradient, to simulate an open, infinite-acting formation system and avoiding non-physical interference on the near-wellbore seepage field from boundary effects. In the temperature field, the wellbore was set to a constant temperature to represent the continuous heat exchange within the circulating drilling fluid. The far-field boundary maintained the initial temperature distribution determined by the regional geothermal gradient. For the hydration field, the boundary conditions were defined analogously to heat diffusion. The wellbore wall was assigned the saturated water content, while the far-field was fixed at the initial natural water content. The initial model state was configured to represent the original in-situ conditions before drilling.

Several idealizations were employed to focus on core multiphysics coupling mechanisms and clarify the applicability of the results. In the seepage field, the dynamic formation of mud cake at the wellbore wall and its significant retarding effect on pressure transmission were not considered. Therefore, the

simulated pressure response timescale primarily reflects the intrinsic permeability of the rock mass, representing a conservative case without an effective barrier. Additionally, the complex chemo-physical process of hydration was simplified into a phenomenological model controlled by an equivalent diffusion coefficient. Mechanical parameters of the rock formation were assumed homogeneous and isotropic, neglecting the heterogeneity and anisotropy of real sedimentary formations. Despite these simplifications, the model effectively reveals the fundamental coupling laws and response characteristics under pressure, temperature, and hydration effects, providing an internally consistent dataset for the subsequent training of the PINN.

The numerical mesh was generated using an adaptive refinement strategy based on the physical field gradients. Unstructured triangular elements were used in the near-wellbore region to accurately capture stress and seepage variations in high-gradient zones. The model consists of 6,768 elements, with a minimum mesh quality of 0.6292 and an average mesh quality of 0.8898, meeting the requirements for both convergence and accuracy. Fig. 2 illustrates the geometry, coupled physics structure, and adaptively refined mesh of the established 2D multiphysics numerical model.

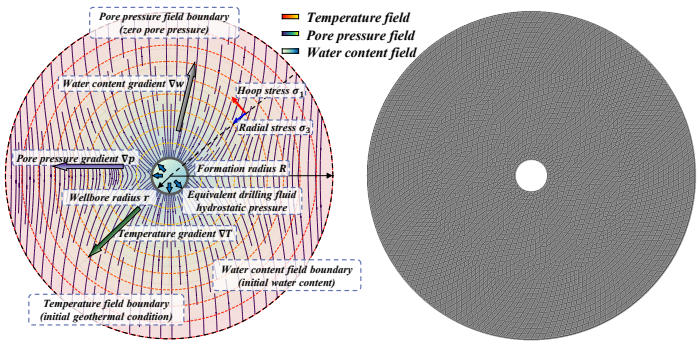


Figure 2: 2D multiphysics model of the wellbore plane and its mesh division.

3.3. COMSOL Simulation

To systematically evaluate the impact of formation property and drilling parameter uncertainties on open-hole wellbore stability, parameter variation ranges covering typical sandstone and mudstone characteristics were constructed. This was based on measured logging data and core experiment results from the Caofeidian block in China's Bohai Sea. A high-dimensional input perturbation scheme was then designed using Latin Hypercube Sampling (LHS) to achieve an effective and uniform exploration of the global parameter space McKay et al. (2000).

Considering the significant lithological heterogeneity in this block, a stratified sampling strategy was introduced into the LHS design to accurately capture the distribution characteristics of the physical and mechanical properties of sandstones and mudstones Lohr (2021). This strategy ensures that samples are uniformly distributed within each lithological sub-interval, significantly enhancing the model's ability to express coupled responses in multi-lithology open-hole sections and improving the generalization of subsequent predictions. A total of 3,000 input samples were generated, covering over 30 key parameters. The parameter ranges, shown in Table 1, account for regional differences in diagenesis, cementation, mineral composition, pore structure, and in-situ temperature and pressure conditions, ensuring that the model inputs are both representative and practically applicable.

During the high-fidelity numerical simulations, a total of 1910 sets of converged solutions were successfully generated. The output variables include the spatio-temporal distributions of equivalent stress and plastic strain fields. Some samples failed to converge due to boundary conflicts or gradient discontinuities under highly nonlinear coupling conditions and were therefore excluded. The resulting simulation sequences cover typical wellbore exposure evolution modes, providing strong physical constraints for subsequent training of the Bayesian physics-informed network and a reliable data basis for casing setting time decisions.

Fig. 3 shows the 2D evolution of Von Mises stress and plastic strain around the wellbore, revealing the coupled stress–strain response under multiphysics effects.

Fig. 3(a) shows that during the first 100 h of evolution, the surrounding rock undergoes significant stress reconstruction. Starting from the initial stress concentration state at $t = 0$ h (max $\approx$ 80 MPa), the stress state rapidly approaches the yield envelope due to the continuous coupling of multiphysics disturbances. This process peaks at approximately $t = 100$ h, forming a distinct "ring-shaped stress cap", with the maximum equivalent stress increasing to 102.96 MPa. Between 100 and 400 h, the stress growth is effectively suppressed as the plastic zone forms and expands. The system then enters a stabilization phase dominated by stress relief and redistribution, and the local high-stress concentration gradually dissipates.

Correspondingly, the evolution of the plastic strain field, shown in Fig. 3(b), records the transition of the rock mass from elastic to plastic deformation. In the early stage, the rock is mostly in an elastic state, with nearly zero plastic strain. As the stress peaks and triggers rock yielding around 100 h, the plastic strain increases rapidly, reaching its maximum value of 6.90%, marking the onset of macroscopic plastic damage. During the 100–400-h period, although the stress field stabilizes, plastic deformation continues to accumulate, with the strain value eventually increasing to 8.37%. The extent of the plastic zone largely stabilizes during this phase, forming a relatively closed plastic damage zone. This indicates that rock failure has transitioned from a rapid expansion phase to a slow, localized yield accumulation phase.

The coupled evolution of stress and plastic strain demonstrates the two-stage characteristics of the wellbore instability process. It begins with an early, rapid failure stage driven by multiphysics disturbances, followed by a long-term stabilization stage dominated by the rock's internal stress adjustment and plastic flow. These results confirm the physical plausibility of the aforementioned coupled stress–strain response mechanism.

Table 1: Parameter sampling for formations in the Caofeidian block, Bohai Sea, China.

Parameter Name	**Unit**	**Sandstone**	**Mudstone**
Elastic Modulus	MPa	15640–30960	9600–14400
Poisson's Ratio	-	0.20–0.28	0.25–0.35
Biot's Coefficient	-	0.8–1.0	0.6–0.8
Initial Porosity	-	0.12–0.16	0.07–0.11
Permeability	mD	2.5–7.5	0.0005–0.002
Rock Thermal Conductivity	W/(m·K)	1.5–2.5	1.0–2.0
Rock Skeleton Compressibility	1/MPa	$(2.0\tilde{}5.0) \times 10^{-5}$	$(4.0\tilde{}6.0) \times 10^{-5}$
Rock Skeleton Specific Heat	J/(kg·K)	680–920	510–690
Fluid Compressibility	1/MPa	$(4.0\tilde{}5.0) \times 10^{-4}$	$(4.0\tilde{}5.0) \times 10^{-4}$
Initial Cohesion	MPa	5–12	1–5
Initial Internal Friction Angle	°	32–38	22–28
Thermal Expansion Coefficient	1/°C	$(3.0\tilde{}4.0) \times 10^{-5}$	$(4.0\tilde{}6.0) \times 10^{-5}$
Initial Water Content	-	0.02–0.04	0.02–0.04
Saturated Water Content	-	0.08–0.16	0.08–0.12
Hydration Diffusion Coefficient	m²/s	$(4.0\tilde{}9.0) \times 10^{-10}$	$(4.0\tilde{}9.0) \times 10^{-10}$
Filtrate Density	kg/m³	980–1020	980–1020
Matrix Density	kg/m³	2500–2700	2500–2700
Filtrate Viscosity	Pa·s	$(2.8\tilde{}3.4) \times 10^{-4}$	$(2.8\tilde{}3.4) \times 10^{-4}$
Filtrate Specific Heat	J/(kg·K)	4000–4400	4000–4400
Hydration Expansion Coefficient 1	-	0	0.02–0.04
Hydration Expansion Coefficient 2	-	0	0.7–0.95

3.4. Simulation Model Validation

To validate the model's physical plausibility and numerical accuracy, Figs. 4–7 illustrate the spatio-temporal evolution of pore pressure, temperature, and water content under continuous drilling-fluid invasion.

Fig. 4(a) shows the radial profile of pore pressure in the surrounding rock, capturing its complete time-series evolution from a local transient disturbance to a global hydraulic equilibrium under sustained high wellbore pressure. Initially, the pressure front propagates rapidly from the wellbore wall to the far-field. At $t = 0$ h, the pressure gradient reaches its theoretical peak at the wellbore wall, followed by continuous, rapid decay as the pressure front broadens and advances. By the late stage ($t = 300$ h), the pressure gradient throughout the region has approached zero, indicating that the system has reached a final equilibrium state at a new pressure level.

Figs. 4(b)–4(e) present the corresponding 2D pore pressure field evolution, further confirming this dynamic process from a spatial perspective. Concentric, circular isobars expand outward from the wellbore sequentially over time. The transition from a dense distribution in the early stage to a sparse one in the late stage visually characterizes the decay of the pressure gradient. Ultimately, the pressure field becomes nearly uniform across the simulation domain, retaining only a slight asymmetry caused by the in-situ stress field. This complete pressure response is highly consistent with the transient diffusion behavior predicted by the classic Biot–Darcy seepage theory, thus validating the model's physical fidelity in simulating coupled fluid-solid dynamics.

The radial profile in Fig. 5(a) systematically reveals the non-steady-state evolution of the surrounding rock temperature field under the combined action of regional geothermal heat and the wellbore cooling effect. The geothermal gradient maintains a high initial temperature in the far-field, while the circulation of drilling fluid creates a persistent heat sink at the wellbore. As time progresses, heat from far-field is continuously transported to the near-wellbore low-temperature zone. This causes the near-wellbore rock temperature to gradually recover from a lower level and reducing the temperature difference with the far-field.

The 2D temperature field distributions in Figs. 5(b)–5(e) provide spatial confirmation for this inward heat transport process. Concentric, circular isotherms advance sequentially from the outer boundary of the simulation domain towards the center. The evolution of their spatial density, from dense in the early stage to sparse in the later stage, signifies that the rate of change of the temperature field decreases over time. By the late stage of evolution ($t = 400$ h), a significant temperature difference exists between the near-wellbore and far-field regions, indicating that although the intense initial transient response has subsided, the system is far from a thermal equilibrium. The subsequent evolution is expected to be a longer, slow adjustment process. Overall, this heat-transfer simulation verifies the model's physical accuracy and numerical stability in handling non-steady-state, cross-scale heat exchange problems.

The radial profile in Fig. 6(a) reveals a key characteristic of the water invasion process: it progresses slowly due to the extremely low diffusion rate and limited adsorptive capacity of the rock. In sharp contrast to the rapid, global response of the pressure field, this profile shows that the water invasion front advances with a significant lag over the 400-h evolution, with a very limited depth of influence. The water content of the near-

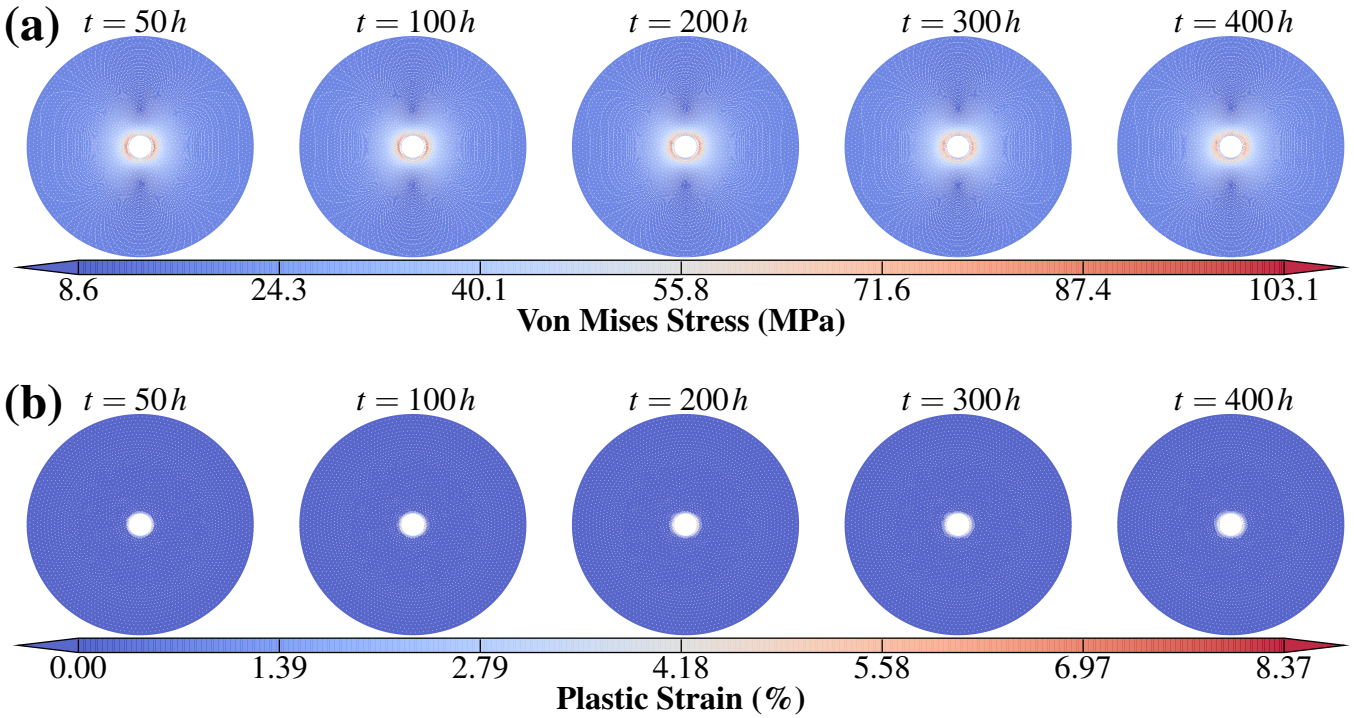


Figure 3: Evolution of the Von Mises stress field and plastic strain field at different times.

wellbore rock increases slowly before stabilizing at a plateau. This phenomenon indicates that rock hydration reaches an inherent equilibrium saturation determined by its microstructure and mineral composition.

The 2D water content fields in Figs. 6(b)–6(e) visually confirm this high degree of localization. The influence of hydration is limited to a thin annular zone immediately surrounding the wellbore wall. Despite its local spatial influence, this process has a controlling effect on wellbore instability. The near-wellbore annulus, softened by hydration, becomes the structurally weakest zone under stress concentration and can trigger initial fractures. Therefore, the model's ability to capture this limited diffusion and local softening process provides a reliable physical basis for wellbore stability assessment.

Fig. 7 further analyzes the water invasion process from the temporal perspective, showing the time series of water content at different radial locations. The curves clearly indicate that the rate of increase in water content is strongly correlated with the distance from the wellbore wall. The monitoring point immediately adjacent to the wellbore responds most rapidly and exhibits the largest increase. As the radial distance increases, the response lag becomes more pronounced and the total increase diminishes, reflecting the inherent attenuation of the diffusion process. The brief dip in water content observed during the early stage ($t < 4$ h) is a transient numerical artifact caused by abrupt initial conditions and dissipates quickly. Subsequently, all locations enter a stable, monotonic growth phase. The progressively decreasing slope of each curve indicates that the water content asymptotically approaches the aforementioned inherent equilibrium saturation.

Figs. 4–7 show the model accurately reveals the spatio-temporal evolution of pore pressure, temperature, and water content under continuous drilling fluid invasion, using both 1D profiles and 2D field distributions. Its characterization of the rapid pressure response, slow thermal exchange, and highly localized hydration process demonstrates good physical consistency within the theoretical framework. This validates the model's high fidelity and physical correctness in simulating multiphysics-coupled instability of open-hole wellbores, providing a reliable data and mechanistic basis for subsequent intelligent modeling.

4. Hierarchical Bayesian Physics-Informed Network Development

4.1. Model Architecture

4.1.1. Network Architecture Design

An HBPINN architecture was designed to efficiently simulate the wellbore wall's state evolution under multiphysics disturbances and enable probabilistic risk inference. This architecture is based on PINNs, a class of deep learning methods that fuse physical constraints with data-driven features Raissi et al. (2019). By integrating the residuals of partial differential equations (PDEs), boundary conditions (BCs), and initial conditions (ICs) into the loss function, PINNs can perform "weakly supervised" learning using only physical prior information, even when labeled data is sparse or absent. This characteristic gives them a significant advantage over traditional data-driven neural networks in complex geological engineering problems, where data acquisition is expensive and information is incomplete.

The basic principle of a PINN is to construct a deep neural network $u_{\Theta_{NN}}(x,t)$, characterized by learnable parameters Θ_{NN},

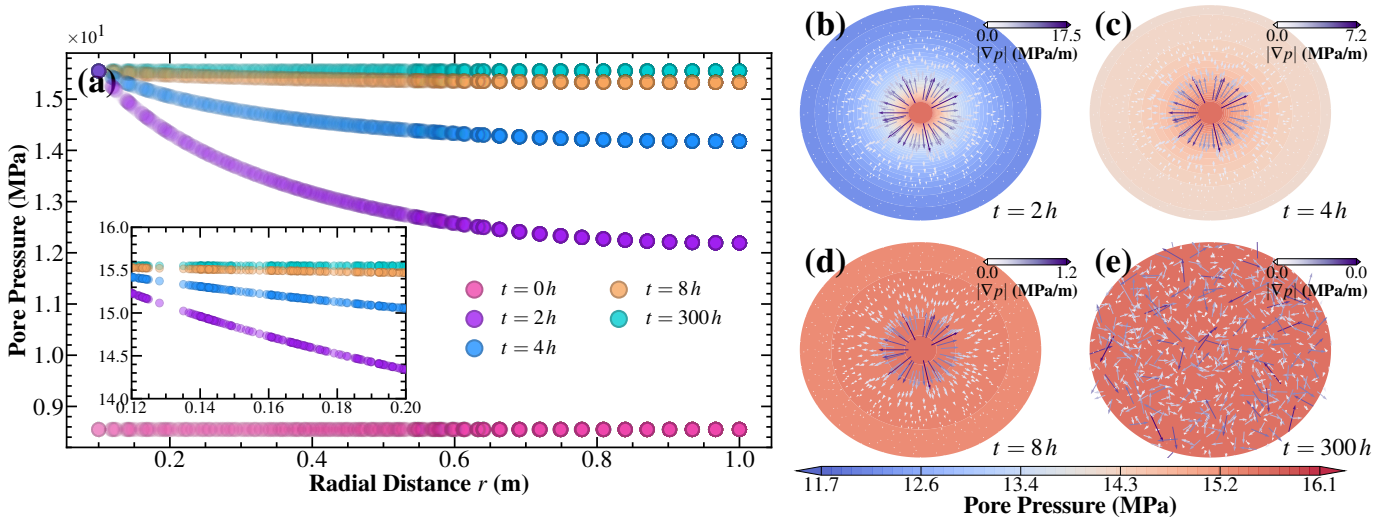


Figure 4: Radial pore pressure distribution and evolution of the pore pressure field at different times.

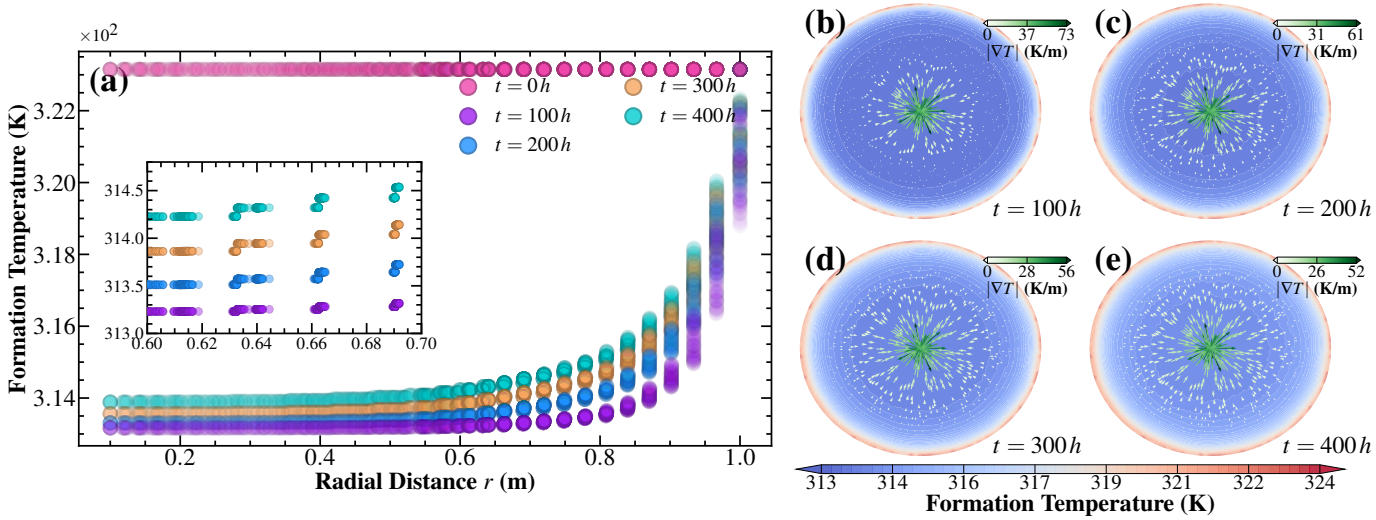


Figure 5: Radial temperature distribution and evolution of the temperature field at different times.

to approximate the solution of a multiphysics problem. The network takes a spatio-temporal coordinate vector $\mathbf{x} = (x, y, t)$ as input and outputs the corresponding state variable vector $\mathbf{u} = (p, T, w, \sigma_{\text{eq}}, \varepsilon_p)$. Using automatic differentiation, derivatives of $\mathbf{u}$ with respect to x and t are computed, and the residuals of the governing physical equations are formulated as a core loss term to constrain network training. Structurally, PINNs typically employ a fully connected feedforward neural network (FNN), with forward propagation following the recursive relation Goodfellow et al. (2016):

$$\begin{cases} \mathbf{a}^l = \mathbf{W}^l \mathbf{z}^{(l-1)} + \mathbf{b}^l \\ \mathbf{z}^l = \sigma(\mathbf{a}^l) \\ \mathbf{f}_{NN} = \mathbf{W}^{(L+1)} \mathbf{z}^L + \mathbf{b}^{(L+1)} \end{cases} \tag{12}$$

where $\mathbf{W}^l$ and $\mathbf{b}^l$ are the weight matrix and bias vector of the l-th layer, respectively; $\sigma(\cdot)$ is the activation function; L is the total number of hidden layers; and $\mathbf{f}_{NN}$ is the final output. Through backpropagation and optimization algorithms such as gradient descent, the network parameters are iteratively adjusted so that the output approximates observational data while satisfying the governing physical equations and constraints.

The loss function of a PINN typically includes multiple components to simultaneously represent different physical laws and boundary conditions:

$$L_{\text{total}} = \omega_f L_{\text{PDE}} + \omega_b L_{\text{BC}} + \omega_0 L_{\text{IC}} + \omega_d L_{\text{Data}} \tag{13}$$

where L_{PDE} is the mean squared error of the governing equation residuals at selected collocation points; L_{BC} and L_{IC} represent the residuals for boundary and initial conditions, respectively; and L_{Data} is the fitting error for available labeled data. Weighting coefficients ω balance the contributions of each loss term during the training process.

The calculation of the L_{PDE} residual term relies on automatic differentiation (AD) Baydin et al. (2018). The partial derivatives of the network output with respect to its input variables are obtained directly through the chain rule via the backpropagation mechanism, without explicitly constructing finite difference schemes or symbolic expressions. This approach signif-

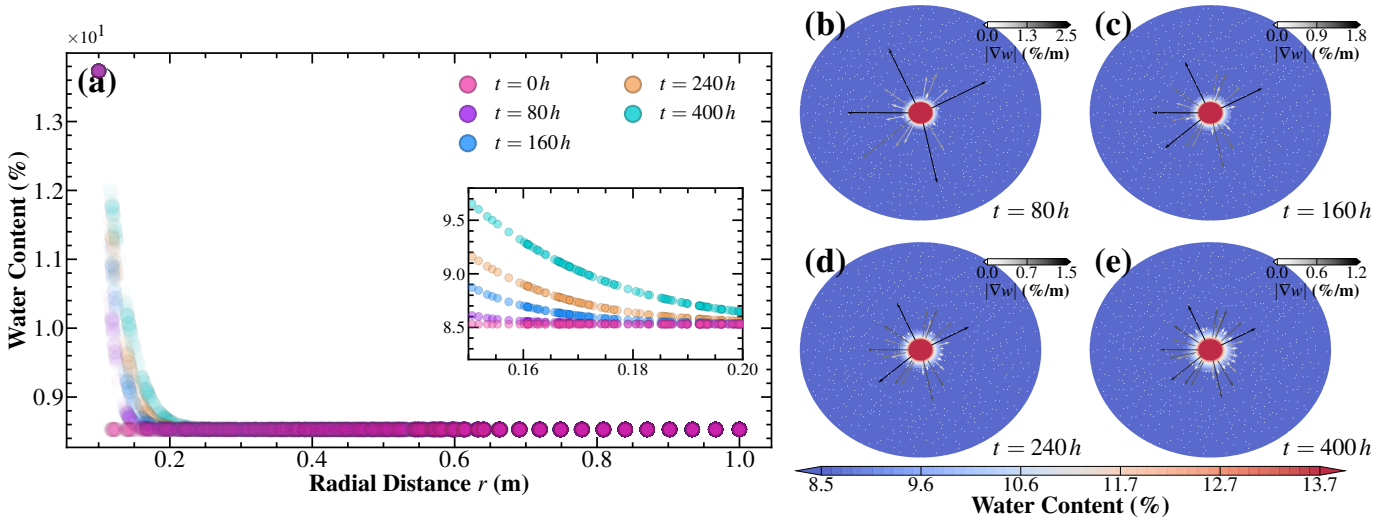


Figure 6: Radial water content distribution and evolution of the water content field at different times.

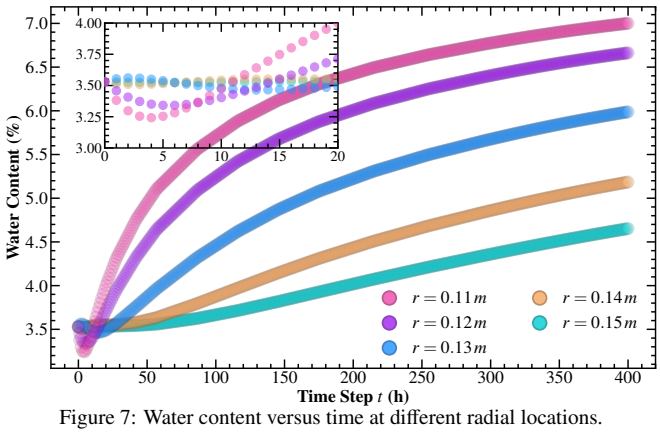


Figure 7: Water content versus time at different radial locations.

icantly enhances the efficiency and precision of the differentiation. It makes PINNs particularly advantageous for handling multiphysics coupling problems that involve high-order derivatives or strong nonlinearities, making them well-suited for constructing and solving complex PDE-governed models.

In terms of training strategy, PINNs use a "weakly supervised" mechanism based on collocation points. The PDE residual is treated as a training objective distributed across the computational domain. This approach avoids the numerical stability requirements and memory burdens of traditional grid-based solvers, enabling good performance in unstructured domains, complex BCs, and nonlinear degradation problems. Furthermore, observational data or numerical simulation results can be flexibly incorporated during training. The L_{Data} term strengthens the model's ability to fit local regions, boundary behaviors, or key time points, enhancing adaptability to real-world geological conditions.

Based on these principles, the HBPINN architecture extends the standard PINN framework by introducing a multi-branch physics prediction structure alongside a Bayesian inference mechanism. It independently designs neural network sub-modules for the four major physical processes: seepage, heat transfer, hydration diffusion, and elasto-plastic mechanics. These modules are trained jointly using a unified governing equation residual loss, ensuring coupling consistency between physical fields. Simultaneously, a Bayesian updater module performs posterior inference on formation parameters based on the PINN's predictions, quantifying key parameter uncertainties.

Seepage Prediction Head: This head solves the governing equations for pore pressure p. Training is primarily driven by PDE residuals to achieve physics-driven learning. Additionally, a small amount of pressure data from COMSOL Multiphysics can be introduced as a data supervision term to enhance fitting accuracy in specific regions.

Thermal Prediction Head: Based on the heat transfer equation, this head uses the thermal diffusion residual, generated by automatic differentiation of the temperature T with respect to the spatio-temporal coordinates, as the primary training constraint to simulate non-steady-state heat transfer between the wellbore and formation.

Hydration Prediction Head: Responsible for predicting the water content w, this head constructs a diffusion-based loss term similar to the thermal head. It uses a low diffusion coefficient as a constraint to enhance the model's ability to capture the delayed hydration near the wellbore wall. To prevent "learning leakage," neither the hydration nor thermal heads use gradient labels from simulation data during training; their physical learning path is constructed solely from initial/boundary values and equation residuals.

Mechanics Output Head: This head couples the Drucker–Prager yield criterion with the elasto-plastic constitutive model. It uses the predicted w and T to dynamically update the rock's mechanical parameters, subsequently outputting equivalent stress σ_{eq} and plastic strain ε_p. The output of this module is constrained by the mechanical governing equation residuals and can be compared with results from COMSOL Multiphysics to validate its predictive accuracy.

Bayesian Updater: This component forms the core of the network's uncertainty expression mechanism. Its primary func-

tion is to use the PINN's predictive outputs to evaluate a likelihood function based on physical criteria. Combined with the parameters' prior distributions, it performs posterior sampling of key formation parameters using MCMC methods, quantifying their predictive uncertainty and providing confidence levels for decision-making.

This multi-branch collaborative structure enables the HBPINN to capture both multiphysics interactions and the joint uncertainties of state variables and formation parameters. It provides a foundational model for the state evolution of an open-hole wellbore wall under multiphysics disturbances. The overall structure is illustrated in Fig. 8.

4.1.2. Physics Constraint Embedding

To ensure physical consistency and interpretability, residuals of the governing equations are embedded as core loss terms during training. All residuals are computed using AD without the need to explicitly construct finite difference schemes, thus ensuring the numerical stability and physical accuracy of high-order derivative calculations. The design of the residuals strictly follows the proposed coupled seepage–stress–thermal–hydration governing equations, including the seepage-mechanics residual loss, the hydration-thermal diffusion residual loss, the elasto-plastic yield residual loss, and the boundary and initial condition error terms.

For the seepage-mechanics coupled residual, the following constraint is constructed based on Darcy's law and mass conservation:

$$L_p = \left\| \frac{\partial}{\partial x}\left(\frac{\rho_w k}{\mu_0}\frac{\partial p}{\partial x}\right) + \frac{\partial}{\partial y}\left(\frac{\rho_w k}{\mu_0}\frac{\partial p}{\partial y}\right) + \phi\rho_w\gamma_l\frac{\partial p}{\partial t} + \rho_w\frac{\partial \phi}{\partial t}\right\|_2^2 \tag{14}$$

where L_p is the seepage-mechanics residual loss term (dimensionless). This constraint reflects the spatial diffusion, temporal evolution, and response to porosity changes of the pore pressure in a 2D porous medium. The network computes the derivatives of p with respect to space and time via AD and incorporates the porosity evolution function based on volumetric strain (see Eq. (10)) to ensure the dynamic consistency of the coupled response between pore pressure and skeleton deformation.

The hydration–thermal diffusion residual loss consists of a heat-conduction-like hydration model and a non-steady-state heat transfer governing equation, expressed jointly as:

$$L_{wT} = \left\| \frac{\partial w}{\partial t} - D\left(\frac{\partial^2 w}{\partial x^2} + \frac{\partial^2 w}{\partial y^2}\right)\right\|_2^2 + \left\| (\phi\rho_w C_M + (1-\phi)\rho_s C_s)\frac{\partial T}{\partial t} - (\rho_w C_M)\frac{k}{\mu_0}\nabla p\cdot\nabla T - \nabla\cdot(\lambda_{\text{eff}}\nabla T)\right\|_2^2 \tag{15}$$

where L_{wT} is the joint hydration-thermal diffusion residual loss (dimensionless). The first term describes the spatio-temporal diffusion of water content w, while the second term constrains the complete energy conservation process, including the combined heat capacity of the rock-fluid system, fluid convection, and effective thermal conduction in the porous medium. To improve the physical distinguishability, thermal gradient and water content data from COMSOL Multiphysics were not used during training; the network learned the physics solely from the boundary/initial conditions and the equation residuals.

The elasto-plastic yield residual loss uses the standard form of the Drucker–Prager yield criterion to construct the constraint function:

$$L_y = \|aI_1 + \sqrt{J_2} - k\|_2^2 \tag{16}$$

where L_y is the elasto-plastic yield residual loss (dimensionless); I_1 and J_2 are the first stress invariant and the second deviatoric stress invariant, respectively, whose definitions and calculation methods are inherited from Eq. (5); and a and k are the Drucker–Prager yield surface parameters, defined as Alejano and Bobet (2014):

$$\begin{cases} a = 2\sin\phi(w)/\left(\sqrt{3}(3-\sin\phi(w))\right) \\ k = 6c(w)\cos\phi(w)/\left(\sqrt{3}(3-\sin\phi(w))\right) \end{cases} \tag{17}$$

where $c(w)$ is the cohesion function controlled by water content (MPa), and $\phi(w)$ is the internal friction angle function controlled by water content (°). In the above yield function, cohesion $c(w)$ and internal friction angle $\phi(w)$ are dynamically adjusted according to Eq. (7), ensuring that the mechanics module is sensitive to the rock strength evolution under coupled hydration-thermal effects.

In addition to the physics-based residual terms, the boundary condition error L_{BC} and initial condition error L_{IC} are introduced as explicit constraints during training. The boundary condition error is defined as:

$$L_{BC} = \sum_{i=1}^{N_{BC}}\sum_{j=1}^{N_t}\Big[(p_{\text{pred}}(x_i^b,t_j) - p_{BC}(x_i^b,t_j))^2 + (T_{\text{pred}}(x_i^b,t_j) - T_{BC}(x_i^b,t_j))^2 + (w_{\text{pred}}(x_i^b,t_j) - w_{BC}(x_i^b,t_j))^2\Big] \tag{18}$$

where p_{pred}, T_{pred}, w_{pred} are the network's predicted values for pore pressure, temperature, and water content; p_{BC}, T_{BC}, w_{BC} are the true values at the boundary; N_{BC} is the total number of boundary sample points; N_t is the total number of discrete points in the evolution time domain; x_i^b is a spatial sample point on the model boundary; and t_j is a discrete time point during the physical evolution(s). The initial condition error L_{IC} is defined similarly as:

$$L_{IC} = \sum_{i=1}^{N_{IC}}\Big[(p_{\text{pred}}(x_i^0,t_0) - p_{IC}(x_i^0,t_0))^2 + (T_{\text{pred}}(x_i^0,t_0) - T_{IC}(x_i^0,t_0))^2 + (w_{\text{pred}}(x_i^0,t_0) - w_{IC}(x_i^0,t_0))^2\Big] \tag{19}$$

where p_{IC}, T_{IC}, w_{IC} are the true values at the initial time; N_{IC} is the total number of initial condition sample points; t_0 specifi-

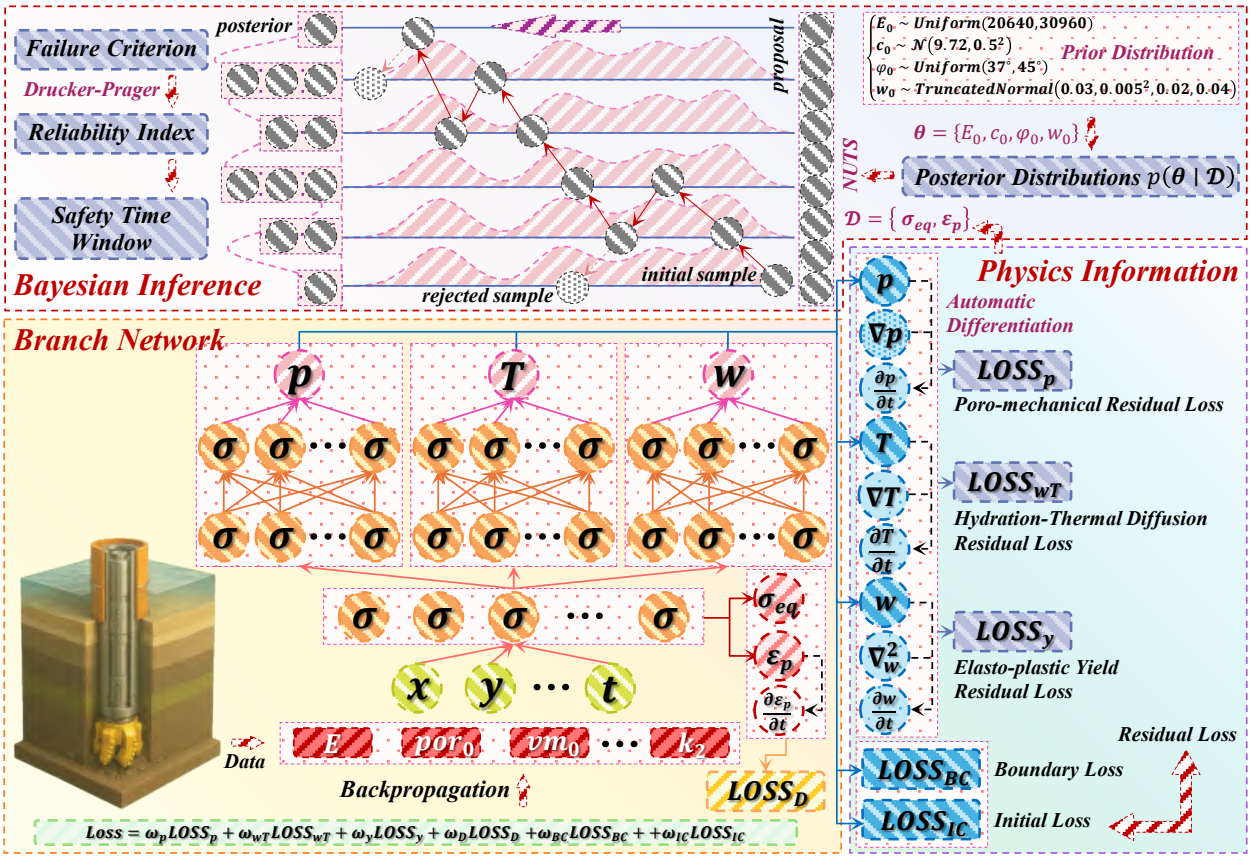


Figure 8: HBPINN architectural diagram.

cally refers to the start time of the physical evolution(s); and x_i^0 is a spatial sample point at the initial time.

This approach ensures that during training, the HBPINN considers both the physical constraints and maintains consistency with the initial and boundary conditions, thereby enhancing the model's physical plausibility and predictive accuracy.

4.1.3. Bayesian Inference

To model the uncertainty of key formation parameters and conduct a probabilistic assessment of failure risk during wellbore state evolution, a Bayesian inference mechanism was introduced into the HBPINN framework. This mechanism consists of two stages: a parameter posterior inference stage based on physical constraints, and a risk quantification stage based on engineering criteria. This design allows the model to quantitatively predict wellbore instability risk while maintaining physical consistency.

The inference process begins with selecting key formation parameters and specifying prior knowledge. The set of parameters to be inferred, θ, was selected based on their influence on wellbore stability:

$$\theta = \{E_0, c_0, \phi_0, w_0\} \tag{20}$$

where E_0 is the initial elastic modulus (MPa); c_0 is the initial cohesion (MPa); ϕ_0 is the initial internal friction angle (°); and w_0 is the initial water content (dimensionless).

Based on the formation parameter statistics from Table 1, the following prior distributions $p(\theta)$ were assigned:

$$\begin{cases} E_0 \sim U(20640, 30960) \\ c_0 \sim \mathcal{N}(9.72, 0.5^2) \\ \phi_0 \sim U(37°, 45°) \\ w_0 \sim \mathcal{TN}(0.03, 0.005^2; 0.02, 0.04) \end{cases} \tag{21}$$

where $U(\cdot,\cdot)$ denotes a uniform distribution; $\mathcal{N}(\cdot,\cdot)$ denotes a normal distribution; and $\mathcal{TN}(\mu, \sigma^2; a, b)$ denotes a truncated normal distribution.

For parameter inference, an approximate Bayesian computation (ABC) strategy was adopted Sunnåker et al. (2013). An approximate likelihood function was constructed using the residual of the state-dependent Drucker–Prager yield function $F(I_1, J_2)$, whose specific form was defined in Eq. (4):

$$L(\theta) = \exp\left(-\beta \sum_{i=1}^{N} [F^{(i)}(\theta)]^2\right) \tag{22}$$

where $L(\theta)$ is the value of the likelihood function given the parameter set θ (dimensionless); $F^{(i)}(\theta)$ is the yield function residual calculated from parameter θ at the i-th spatial sample point (MPa); β is a scale factor (1/MPa²); and N is the total number of spatial sample points (dimensionless).

By combining the likelihood function with the prior distributions of the parameters, the posterior distribution is constructed

via Bayes' formula Gelman et al. (1995):

$$p(\theta \mid D) \propto L(\theta) \cdot p(\theta) \tag{23}$$

where $p(\theta|D)$ is the posterior probability distribution of the parameters; and D represents the physical state field predicted by the HBPINN, which is used to calculate the yield function residuals. A No-U-Turn sampler (NUTS), an MCMC method, was used to efficiently sample this posterior distribution, yielding a set of posterior parameter samples $\theta^{(i)}$ Hoffman and Gelman (2014).

After obtaining the posterior samples, a failure probability function based on a smooth transition was introduced to establish an evaluation system that aligns with engineering practice while maintaining good mathematical properties. This method first calculates the corresponding equivalent yield stress $\sigma_y^{(i)}$ and equivalent yield strain $\varepsilon_y^{(i)}$ for each parameter sample $\theta^{(i)}$:

$$\begin{cases} \sigma_y^{(i)} = k/a \\ \varepsilon_y^{(i)} = \sigma_y^{(i)}/E^{(i)} + 0.002 \end{cases} \tag{24}$$

where $\sigma_y^{(i)}$ is the equivalent yield stress under the i-th parameter sample (MPa); $\varepsilon_y^{(i)}$ is the corresponding equivalent yield strain (dimensionless); $E^{(i)}$ is the dynamic elastic modulus under the current parameter sample and water content w, as defined in Eq. (7) (MPa); parameters a and k are functions of w, as defined in Eq. (17); and the 0.002 term represents the 0.2% plastic strain offset commonly used in engineering.

Subsequently, the network's predicted equivalent stress and plastic strain is normalized, and an S-shaped logistic function $L(x)$ is introduced to provide a smooth, probabilistic mapping of the failure likelihood:

$$L(x) = \frac{1}{1 + \exp(-b(x - x_0))} \tag{25}$$

where x is the normalized stress or strain value (dimensionless); x_0 is the center point of the mapping function, set to 1 (dimensionless); and b is the slope factor, set to 12 (dimensionless).

Based on this, for any given parameter sample $\theta^{(i)}$, the instantaneous failure probability P_{inst} at a spatio-temporal point (t, x, y) can be constructed as:

$$P_{\text{inst}}(\theta^{(i)}; t, x, y) = 0.4 \cdot L\left(\frac{\sigma_{\text{eq}}^{(i)}}{\sigma_y^{(i)}}\right) + 0.6 \cdot L\left(\frac{\varepsilon_p^{(i)}}{\varepsilon_y^{(i)}}\right) \tag{26}$$

where $P_{\text{inst}}(\theta^{(i)})$ is the instantaneous failure probability under the i-th parameter sample (dimensionless); and $\sigma_{\text{eq}}^{(i)}$ and $\varepsilon_p^{(i)}$ are the equivalent stress (MPa) and equivalent plastic strain (dimensionless), respectively, predicted by the HBPINN under the parameter sample $\theta^{(i)}$.

The final failure probability P_f of the wellbore wall at that spatio-temporal point is defined as the mathematical expectation of the instantaneous failure probability P_{inst} over all posterior samples:

$$P_f(t, x, y) = \frac{1}{N_{\text{samples}}} \sum_{i=1}^{N_{\text{samples}}} P_{\text{inst}}(\theta^{(i)}; t, x, y) \tag{27}$$

where $P_f(t, x, y)$ is the final failure probability of the wellbore wall (dimensionless); and N_{samples} is the total number of posterior samples (dimensionless).

Based on this, the reliability index $R(t, x, y)$ for that spatio-temporal point can be further defined:

$$R(t, x, y) = 1 - P_f(t, x, y) \tag{28}$$

where $R(t, x, y)$ is the reliability of the wellbore wall (dimensionless), with values closer to 1 indicating greater safety.

Finally, in line with the need for a reliability time window, the critical failure time $t_{\text{safe}}(x, y)$ is defined as:

$$t_{\text{safe}}(x, y) = \min\{t \in T \mid R(t, x, y) < 0.95\} \tag{29}$$

where $t_{\text{safe}}(x, y)$ is the earliest evolution time at which the wellbore reliability at location (x, y) first drops below the preset threshold $R_{\text{thresh}} = 0.95$; and T is the total evolution time domain of the model. This metric is used to dynamically identify time points where the instability risk significantly increases during long-term open-hole exposure, enabling proactive warnings and spatio-temporal reliability analysis.

4.2. Model Training

To ensure that the HBPINN model achieves a balance of physical consistency, numerical stability, and convergence efficiency in predicting wellbore stability evolution and quantifying key formation parameter uncertainties, a stage-wise strategy is adopted for the overall training process. First, the backbone network is trained to complete parameter initialization and embed the physical laws. Subsequently, the network architecture is frozen to perform Bayesian inference based on the maximum a posteriori (MAP) estimate, achieving accurate sampling of the posterior parameter distribution and probabilistic modeling of the failure probability structure. The loss function is constructed using a weighted mean squared error structure, composed of residuals from the multi-field governing equations, boundary and initial condition constraint errors, and the fitting error of physical labels from supervisory data. It is expressed as follows:

$$\begin{aligned} L_{\text{total}} = {} & \omega_p \cdot L_p + \omega_{wT} \cdot L_{wT} + \omega_y \cdot L_y \\ & + \omega_{\text{data}} \cdot L_{\text{data}} + \omega_{BC} \cdot L_{BC} + \omega_{IC} \cdot L_{IC} \end{aligned} \tag{30}$$

where L_p represents the seepage-mechanics residual loss, L_{wT} the hydration-thermal diffusion residual loss, L_y the elasto-plastic yield residual loss, L_{data} the supervisory data label error, and L_{BC} and L_{IC} the physical residual terms for the boundary and initial conditions, respectively. The weighting coefficients ω for each loss term are set empirically based on the numerical scale of the different physical field residuals, their gradient sensitivity to parameters, and their contribution to the overall task. The specific values are as follows:

$$\begin{cases} \omega_p = 1.2 \times 10^{-4} \\ \omega_{wT} = 1.1 \times 10^{-12} \\ \omega_y = 2.0 \times 10^{-4} \\ \omega_{\text{data}} = \omega_{BC} = \omega_{IC} = 1.0 \end{cases} \tag{31}$$

The AdamW optimizer is employed, and weight decay and dropout regularization strategies are jointly used to enhance training stability and generalization Loshchilov and Hutter (2017a); Srivastava et al. (2014). The GELU activation function is chosen to facilitate the synergistic convergence of the multiphysics residual terms Hendrycks and Gimpel (2016). The learning rate scheduling strategy uses a three-stage cosine annealing with restarts, with the learning rate η_t at step t defined as Loshchilov and Hutter (2017b):

$$\eta_t = \eta_{\min} + \frac{1}{2}(\eta_{\max}^{(s)} - \eta_{\min})\left[1 + \cos\left(\frac{\pi \cdot t_{\text{cur}}}{T^{(s)}}\right)\right] \tag{32}$$

where $\eta_{\max}^{(s)}$ is the maximum learning rate for stage s; $\eta_{\min}$ is the minimum learning rate during training; and t_{cur} and $T^{(s)}$ are the number of steps already taken in the current stage and the total number of steps in the stage, respectively. The early stopping strategy is introduced during training to monitor the validation set loss in real-time to avoid model overfitting.

In the Bayesian inference stage, the backbone network is frozen, and the NUTS sampler is used for posterior sampling of the parameter set θ. The likelihood function is constructed from the Drucker–Prager yield function residual, and a scale factor β is used to adjust the smoothness of the residual distribution. Initial sampling values are provided by the MAP estimate obtained during the training phase. Convergence efficiency and stability of NUTS are enhanced by setting a number of warm-up steps N_{warm} and a target acceptance rate α_{target}. Table 2 summarizes the core hyperparameter settings for HBPINN model training and Bayesian inference.

The algorithm 3 shows the overall execution logic and operational sequence of the HBPINN algorithm during training iterations and uncertainty inference.

To evaluate the physical consistency fitting performance of the HBPINN model during training, and its generalization capability on unseen samples, Figs. 9 and 10 present the evolution trend curves of the main physical residual terms, boundary condition losses, initial condition losses, and the total loss during the training and validation phases. Considering the differences in magnitude and gradient scale among the governing equation residual terms, each loss branch in the figures has been multiplied by its corresponding weighting coefficients ω to reflect its contribution to optimizing the physical constraints during training.

Fig. 9(a) shows that the three main residual loss terms of the HBPINN model exhibit typical phased convergence characteristics during training. In the initial stage (0–25,000 epochs), the seepage-mechanics residual loss L_p and the elasto-plastic yield residual loss L_y dominate the overall descent. This indicates that the Darcy–Biot governing equations and the elasto-plastic constitutive constraints strongly drive the network's weight adjustments in the early training phase. The rapid decrease in residuals during this stage reflects the model's quick adaptation under the drive of large physical errors. In the middle stage (25,000–70,000 epochs), training enters a stable convergence period, where the hydration-thermal diffusion residual loss L_{wT} reaches its minimum and remains relatively stable. This suggests that the model has completed the initial fitting and convergence for diffusion-type physical mechanisms. In the later stage (70,000–100,000 epochs), the overall residual fluctuations decrease. The variation ranges of L_p and L_y are controlled within ±0.8% and ±1.2%, respectively, indicating that the coupled physical fields have achieved a highly consistent convergence state. Notably, the hydration-thermal residual loss shows a slight upward trend in the final stage, suggesting that this branch is highly sensitive to parameters.

Fig. 9(b) further validates the generalization capability of the above training trends. The evolution of the total loss and each physical residual term on the validation set is highly consistent with the training process, demonstrating robustness to unseen data. However, the minimum loss values for each residual term generally increase by 25%–33%, with L_p and L_y showing minimum deviations of 0.2% and 6.5%, respectively. This validates the high stability of the seepage coupling term based on the Darcy–Biot equation in spatial extrapolation, while also revealing that the elasto-plastic residual is more sensitive to boundary conditions changes. In the later training stage, the validation residual curves for L_p and L_y exhibit slight oscillating upward trends, suggesting slight overfitting under strong physical constraints.

In the training stage shown in Fig. 10(a), the boundary and initial condition losses converge rapidly during the early iterations, decreasing from an initial order of magnitude of 10^{-1} to within 10^{-3}. This reflects the network's efficient perception and integration of boundary and initial information. Additionally, the data fitting loss L_{data} converges quickly in the early stage, dropping from an approximate unit order of magnitude to around 10^{-3}, demonstrating the network's strong ability to represent the labeled samples. In the middle and late stages of training, all three types of losses enter a slow-decline phase with significantly reduced fluctuation ranges, indicating that the supervisory branches of the network have gradually coordinated. By the last stage of training, the total loss L_{total} stabilizes at an order of magnitude of 10^{-3}, showing that the overall training process has good convergence stability and residual control.

Fig. 10(b) shows the loss evolution trend during the validation phase under the same supervisory mechanism. Its overall trend is consistent with the training phase. The boundary and initial condition losses also successfully converge to the 10^{-4}–10^{-3} range. The data fitting loss is slightly higher than in the training set but remains within a low-level fluctuation range. The total loss oscillates stably between 10^{-3} and 10^{-2}, with no obvious signs of divergence.

4.3. Model Evaluation

4.3.1. Model Prediction Performance Evaluation

Fig. 11 and Fig. 12 systematically illustrate the prediction performance of the HBPINN model for key geomechanical responses of the open-hole wellbore wall within a continuous evolution time window of 400 h. Fig. 11 focuses on the spatial distribution of the Von Mises equivalent stress and its error evolution, while Fig. 12 presents the corresponding results for plastic strain.

Fig. 11(a) shows the ground-truth evolution of the Von Mises equivalent stress in the rock surrounding the wellbore under

Table 2: Hyperparameter configuration for HBPINN model training and Bayesian inference.

Symbol	Description	Value
N_{BC}	Number of boundary condition sample points	800
N_{IC}	Number of initial condition sample points	6768
N_R	Number of sample points for each physics residual	6768
N_{data}	Number of supervisory data points	3000
B	Batch size	256
L	Number of hidden layers	6
N_h	Number of neurons per layer	128
$\sigma(\cdot)$	Activation function	GELU
$\omega_p, \omega_{wT}, \omega_y$	Weights for multi-field residual terms	$[1.2 \times 10^{-4}, 1.1 \times 10^{-12}, 2.0 \times 10^{-4}]$
$\omega_{\text{data}}, \omega_{BC}, \omega_{IC}$	Weights for data and boundary terms	[1.0, 1.0, 1.0]
$[T_1, T_2, T_3]$	Steps for three-stage cosine annealing	[25k, 45k, 30k]
$\eta_{\text{stage\_max}}$	Maximum learning rate for each stage	$[1.0 \times 10^{-3}, 5.0 \times 10^{-3}, 2.0 \times 10^{-4}]$
η_{min}	Minimum learning rate	1.00×10^{-5}
λ_{wd}	Weight decay coefficient	1.00×10^{-4}
p_d	Dropout rate	0.2
N_{patience}	Early Stopping patience epochs	5000
δ_{stop}	Early Stopping threshold	1.00×10^{-6}
β	Likelihood scale factor	0.1
N_{mcmc}	Total MCMC sampling steps	2000
N_{warm}	NUTS warm-up steps	300
α_{target}	NUTS target acceptance rate	0.9

continuous multiphysics disturbances. This stress field expands symmetrically in the radial direction from the wellbore center and exhibits dual modes of concentration and expansion at specific stages of evolution. Over time, the dominant stress zone gradually transitions to the outer edge of the wellbore, with the overall distribution maintaining an axisymmetric structure. Fig. 11(b) demonstrate the prediction results of the HBPINN model. It accurately reproduces the main contours and evolution path of the high-stress regions. Fig. 11(c) shows the absolute error distribution map, which reveals the model's error sensitivity in high-gradient regions. In terms of the dynamic evolution of the error, the model maintains the prediction error below 2 MPa for most of the time period, with the largest errors occurring in regions of intense stress change. In the early stage of evolution (t = 1 h), the peak error exceeds 4 MPa, primarily along stress transition zones near the side boundaries of the wellbore, with some regions ($(X, Y) \approx (-0.11, -0.01)$ m) highly overlapping with the stress maxima. As the evolution progresses, the main error peak gradually moves away from the dominant stress path. By the end of the evolution (t = 400 h), the maximum error value reduces to ~3.26 MPa, concentrated in the region of the oblique axis of symmetry at the radial outer edge, showing a clear spatial shifting trend.

Fig. 12(a) depicts the time-series evolution of the plastic strain zone in the rock surrounding the wellbore. Plastic damage accumulates primarily along both sides of the axis of symmetry in the region near the wellbore and intensifies with extended exposure time. The HBPINN prediction results in Fig. 12(b) accurately capture the primary distribution patterns and growth trends of the wellbore's plastic strain. The error distribution map in Fig. 12(c) shows that the prediction error is concentrated in regions where the plastic strain gradient changes significantly. At the early stage (t = 1 h), the peak error reaches ~0.47% in some strain concentration zones ($(X, Y) \approx (-0.09, 0.04)$ m), coinciding with the dominant strain path. From the mid-to-late stages ($t \geq$ 200 h), the location of the maximum error gradually shifts towards the vicinity of the oblique axis of symmetry of the wellbore. Notably, beyond t = 200 h, the region of maximum plastic strain and maximum error progressively separate. This indicates that the prediction stability of the HBPINN model in the dominant strain zone continues to improve over time.

In summary, the HBPINN model demonstrates good spatial recognition capabilities and numerical robustness in predicting the Von Mises equivalent stress of the open-hole wellbore wall, accurately capturing the evolutionary features of high-stress zones. For plastic strain, the model demonstrates excellent spatio-temporal resolution, precisely tracking the dynamic evolution of the dominant plastic deformation path of the surrounding rock. These results provide high-credibility data support for the subsequent overall stability assessment and local instability risk identification in open-hole sections.

4.3.2. Model Extrapolation Performance Validation

To further validate the temporal generalization capability of the HBPINN model in capturing the long-term evolutionary behavior of the open-hole wellbore wall, three evolution time points outside the training window (0–400 h) were selected: t = 450 h, 500 h, and 550 h. The performance of the trained model in predicting the wellbore state was evaluated for extrapolation. A fully connected neural network (FCNN) with the same architecture but without physical constraints was used as a

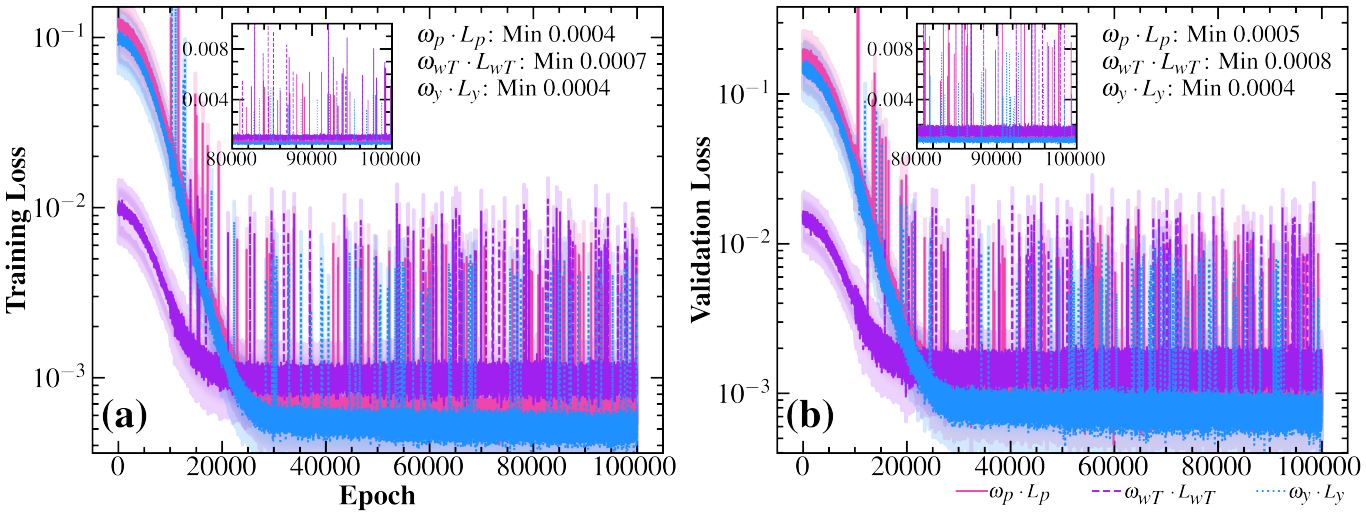


Figure 9: Training and validation loss curves for the main physical residual terms of the HBPINN model.

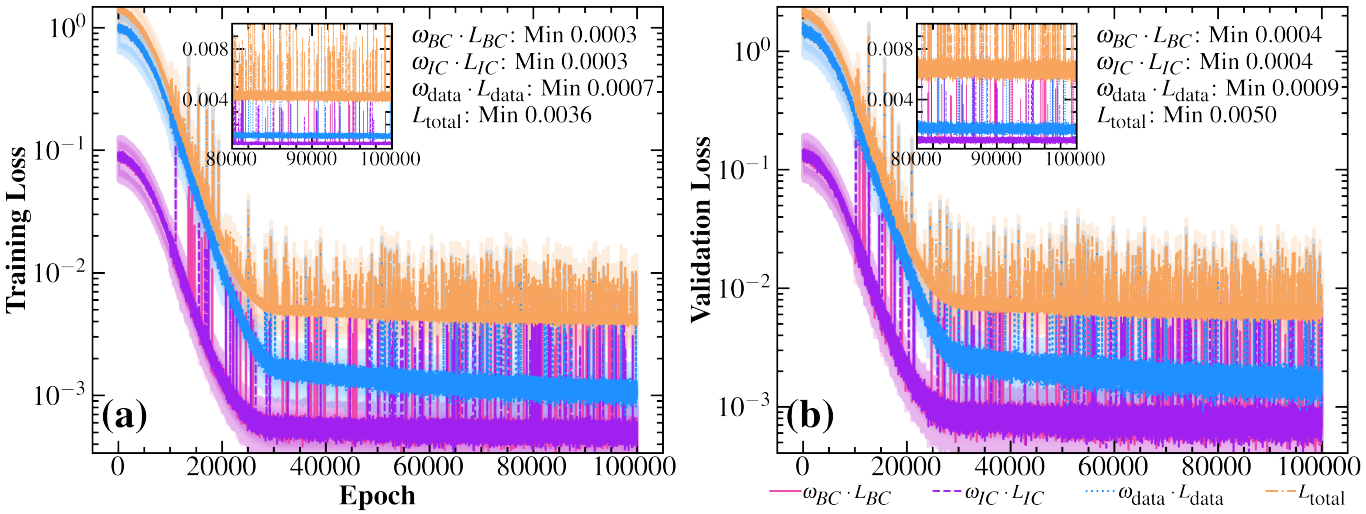


Figure 10: Training and validation loss curves for the boundary condition, initial condition, and data fitting terms of the HBPINN model.

baseline, thereby highlighting the key role of physical information in improving generalization capability. Fig. 13 compares the error time-series evolution and the R^2 performance of the two models in predicting the mechanical field of the wellbore wall.

Fig. 13(a) and (c) collectively reveal the extrapolation performance of the HBPINN model. As shown in Fig. 13(a), the absolute error of the wellbore state exhibits a gradual increase with extrapolation time. This is particularly evident at $t = 500$ h and $t = 550$ h, where error accumulation becomes more pronounced, indicating that long-time-series extrapolation will inevitably lead to a loss of accuracy. In contrast, Fig. 13(c) shows that although the R^2 value of the HBPINN decreases, it consistently remains in a high positive range. Moreover, the error field distribution in the surrounding rock maintains its physical structure. These results indicate that despite error accumulation, the model's predictions for the wellbore state remain stable and physically consistent, without exhibiting non-physical oscillations or divergence.

In contrast, the performance of the FCNN model is completely different. As shown in Fig. 13(b), its predicted mechanical field displays large-scale, unstructured error distributions. This indicates that its predicted stress–strain field severely deviates from the true physical evolution path. The corresponding R^2 value (Fig. 13(c)) rapidly drops to a negative value far below zero. In regression evaluation, this typically indicates that the model has failed, with predictive performance worse than using the average value.

The comprehensive comparison proves that incorporating physical constraints is key to enhancing the model's ability to predict the long-term evolutionary behavior of the open-hole wellbore wall. Although the prediction accuracy of the HBPINN decreases with extrapolation time, it maintains stable and physically consistent predictions. In contrast, the FCNN, lacking physical constraints, exhibits catastrophic performance degradation when facing unknown evolution stages outside the training domain. This demonstrates that the HBPINN possesses superior generalization capability and reliability for long-term

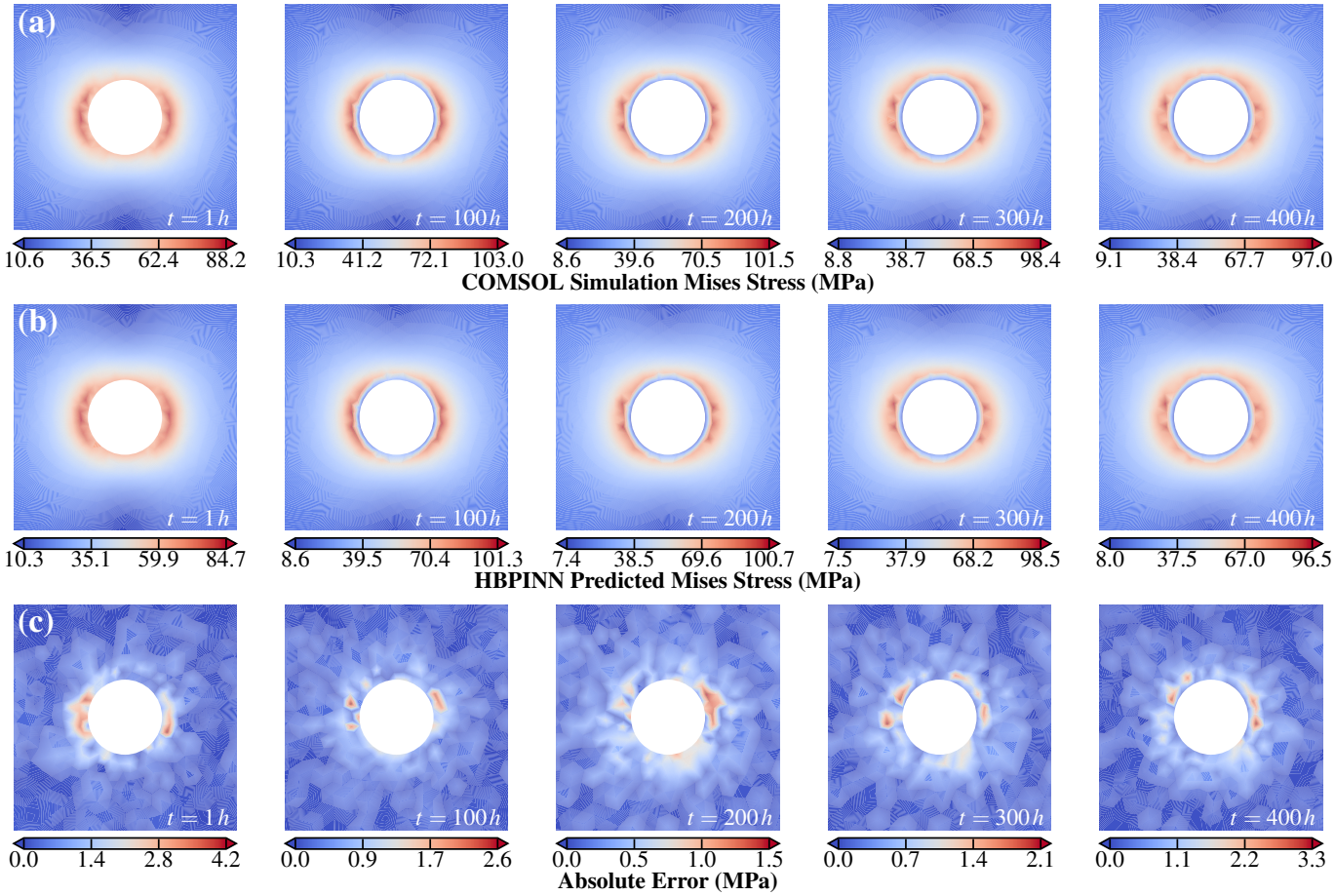


Figure 11: Spatial distribution of Von Mises stress prediction results and error field evolution for the HBPINN model.

stability prediction of open-hole wellbore sections.

4.3.3. *Wellbore Instability Probability and Reliability Index Evolution*

Figs. 14 and 16 presents the reliability assessment and risk analysis of the HBPINN model's predictions for the wellbore stability of an open-hole section at a depth of 528 m. These results quantify the temporal evolution and spatial distribution of instability risk under full-cycle exposure conditions. The analysis focuses on the evolution trend of the global wellbore stability, the earliest failure times of local high-risk zones, and the time-series variation of their reliability indices.

Fig. 14(a) shows the evolution of the average reliability index predicted by the HBPINN model for the open-hole section at this depth. Over the 400-h period, the average reliability gradually decreases from 0.9674 to 0.9637, showing a slight but continuous degradation trend. As time progresses, the gap between the 5% and 95% quantiles gradually widens, and the dispersion of the reliability distribution increases significantly. At the end of the evolution (t = 400 h), the overall system reliability reaches its lowest value, indicating a cumulative degradation of the open-hole section's stability under continuous exposure. At key stages (100–400 h), the average reliability decreases only by 0.0028. However, the 5% quantile remains fixed at 0.6000, indicating that local weak zones persistently experience high instability risk. This result reflects that even though the average reliability at this depth remains high, local areas may have already triggered instability mechanisms.

Fig. 14(b) presents the distribution of earliest failure times predicted for different spatial points in the open-hole section at this depth. The 95% confidence interval ranges from 12.53 to 334.72 h, defining the acceptable exposure time window for this well section. The earliest effective instability prediction occurs at the 12th hour of evolution, suggesting that in the casing setting strategy, long-term open-hole exposure before this time point should be avoided. Furthermore, failure points are primarily clustered in the southwest quadrant of the wellbore (x < 0.5 m, y < 0.5 m), showing clear spatial concentration characteristics.

Fig. 16(a) quantifies the distribution of instability probability across the spatial domain of the open-hole section at this depth. Using a threshold of 0.3, a total of 260 high-risk spatial points are identified, accounting for ~7.5% of the total points. Among these high-risk points, the highest instability probability reaches 1.0000, and the average is 0.9854, indicating strong model consistency for such points. Notably, these high-risk points show significant spatial clustering, highly consistent with the earliest failure region identified in Fig. 14(b).

Fig. 16(b) tracks the evolution of the reliability index for the top five high-risk points. All points display monotonic de-

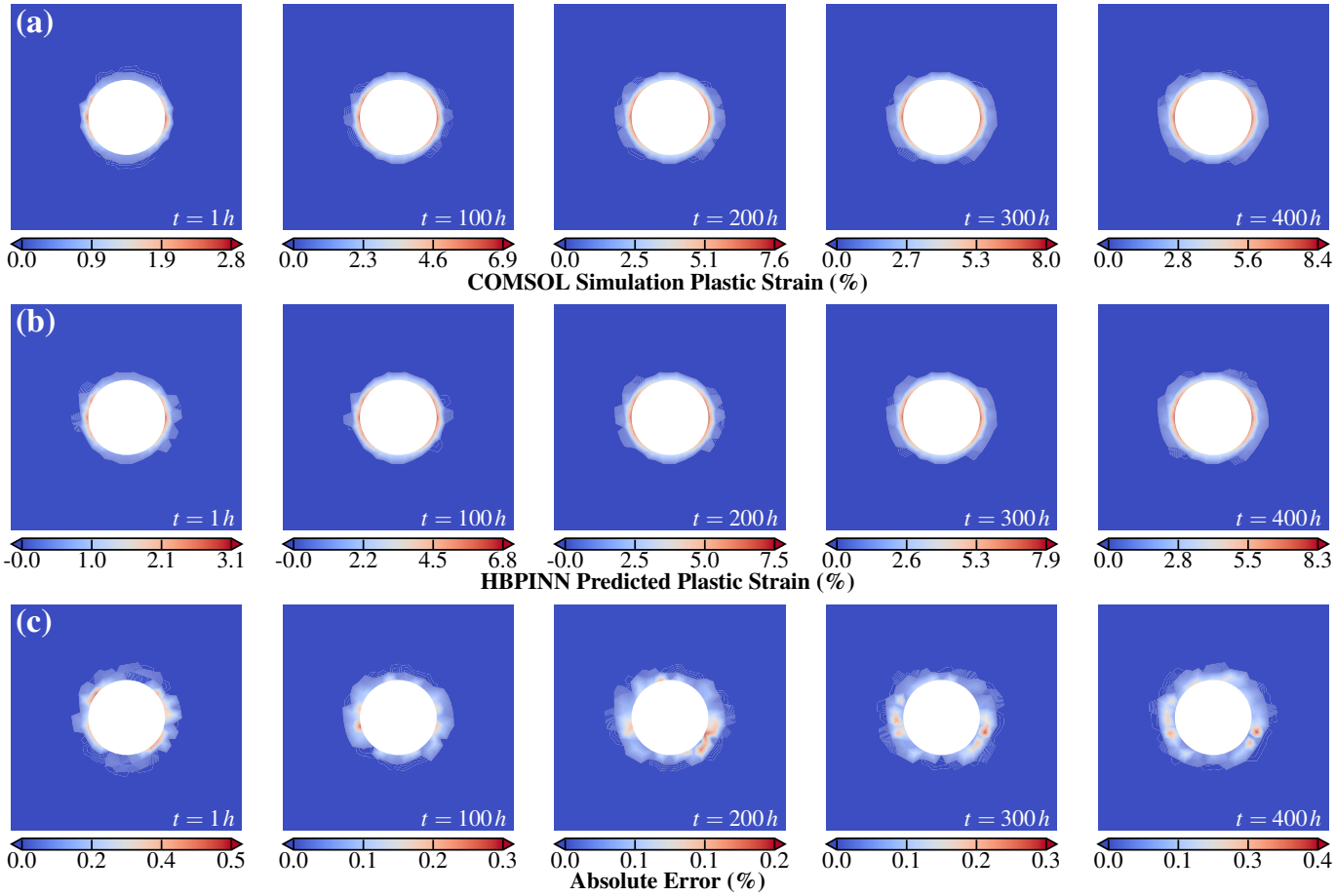


Figure 12: Spatial distribution of plastic strain prediction results and error field evolution for the HBPINN model.

creases, though with different onset times. The reliability of the point [-0.2437, 0.0332] drops to 0.8800 by the 244th hour of evolution, whereas the lowest reliability for the point [-0.2350, 0.0754] occurs near the end of the period at the 397th hour. This indicates that different points exhibit significantly different time sensitivities of their instability potential under long-term exposure. Furthermore, the point [-0.2552, -0.0245], despite starting with a high reliability of 0.9700, drops to 0.9280 at the 304th hour, suggesting its potential evolution into a weak point under long-term multiphysics effects. Overall, high-risk points show an asynchronous evolution, underscoring the limitations of assessing open-hole stability risk at a single moment in time and emphasizing the necessity of conducting dynamic, spatio-temporal joint reliability assessments.

4.3.4. Sensitivity and Interpretability Analysis

SHAP and local sensitivity analysis were employed to quantify how parameter uncertainty contributes to instability risk and affects the predicted failure probability. Key formation parameters considered include the initial elastic modulus, initial cohesion, initial internal friction angle, and initial water content.

Fig. 15 presents the combined analysis results of the mean absolute SHAP values and local sensitivity indices. It shows that the initial water content has the greatest impact on the model's equivalent stress output, with a SHAP value of 1.4613, whereas the initial elastic modulus shows a lower contribution at 0.3124. This indicates that water content plays a crucial role in the deformation and seepage processes of the rock mass. Under long-term open-hole exposure, the changes in water content from cumulative hydration swelling significantly alter the stress state of the wellbore wall. Therefore, the initial water content shows a strong global influence in the SHAP analysis, indicating its dominant role in the variations of permeability and mechanical properties of the geomaterial.

In contrast, the local sensitivity analysis shows that the initial elastic modulus has the largest contribution to the fluctuation of the instability probability, with a sensitivity index of 0.5248. This reflects its role in governing the rock's ability to deform elastically under stress. During drilling, the rock's ability to resist deformation directly affects the stability of the wellbore wall. Especially in deep formations, as pore pressure changes, the amount of deformation and the failure mode of the rock mass are significantly influenced by the initial elastic modulus. Therefore, its contribution to the instability probability is prominent in the local sensitivity analysis.

The difference between these two analyses reveals the different focuses of SHAP and local sensitivity analyses in parameter impact assessment. The SHAP analysis focuses on global contributions, emphasizing the dominant role of initial water

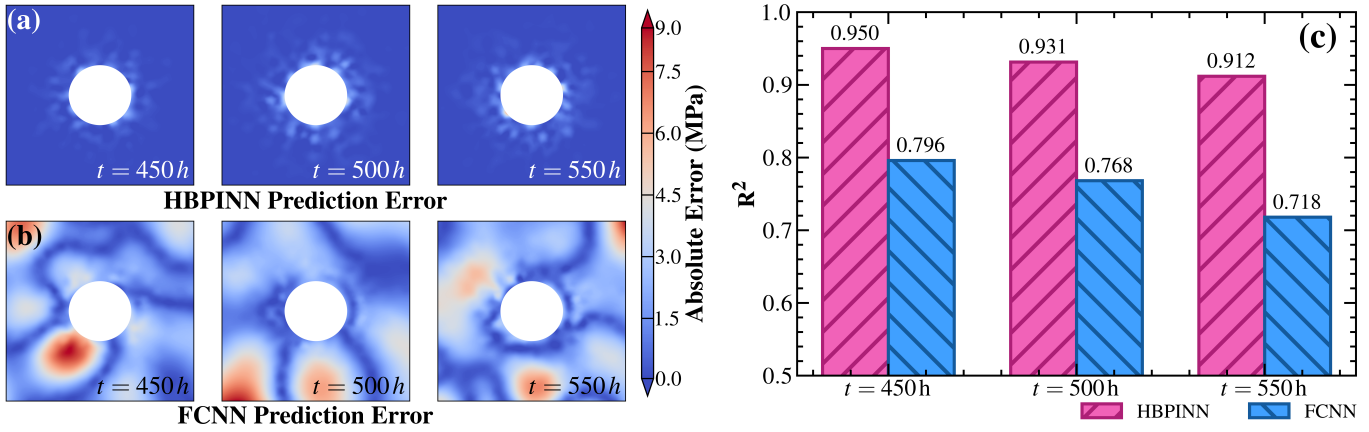


Figure 13: Comparison of error field evolution and R^2 for the HBPINN and FCNN models in time extrapolation.

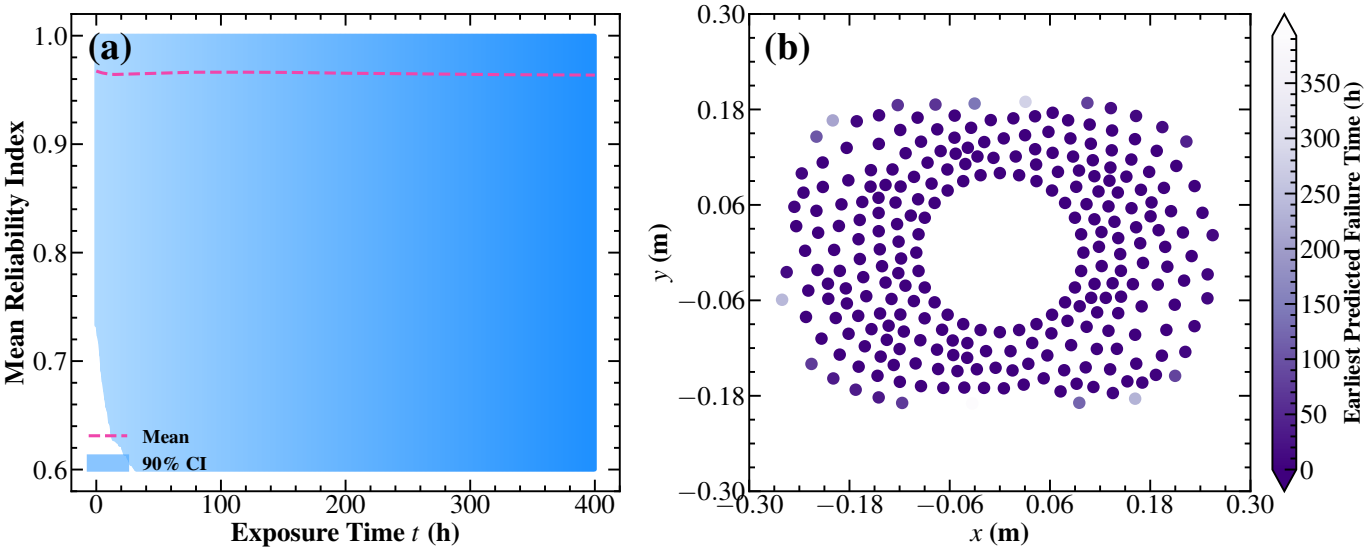


Figure 14: Evolution of average reliability and distribution of earliest failure time for the open-hole section at 528 m depth, predicted by the HBPINN model.

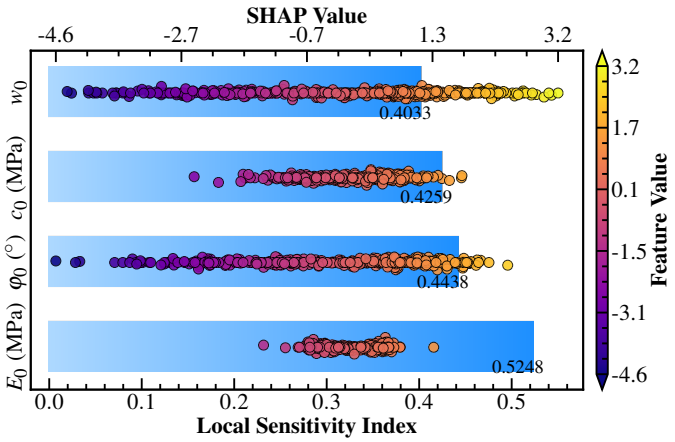


Figure 15: Feature importance and local sensitivity indices of four key formation parameters in the HBPINN model.

content in driving stress concentration through hydration effects during long-term exposure. Local sensitivity analysis, however, captures condition-specific effects, identifying the initial elastic modulus as the key determinant of instability probability, especially in high-risk areas where the influence of the initial elastic modulus on wellbore instability far outweighs that of other parameters.

5. Case Study

To evaluate the predictive capability of the HBPINN model for the wellbore stability evolution process under complex multiphysics disturbances, an 809–910 m open-hole section of a well in the Caofeidian block was selected as a case study. This section is in the third drilling phase, the well was drilled from 809 to 2926 m, while the preceding second section was completed at 808 m. Since it was not supported by casing, its stability was primarily influenced by pore pressure evolution, formation temperature gradients, hydration diffusion effects, and geomechanical parameters, all induced by drilling fluid invasion. Therefore, an early-warning instability analysis was performed based on the measured lithology and the formation's mechanical parameter profile.

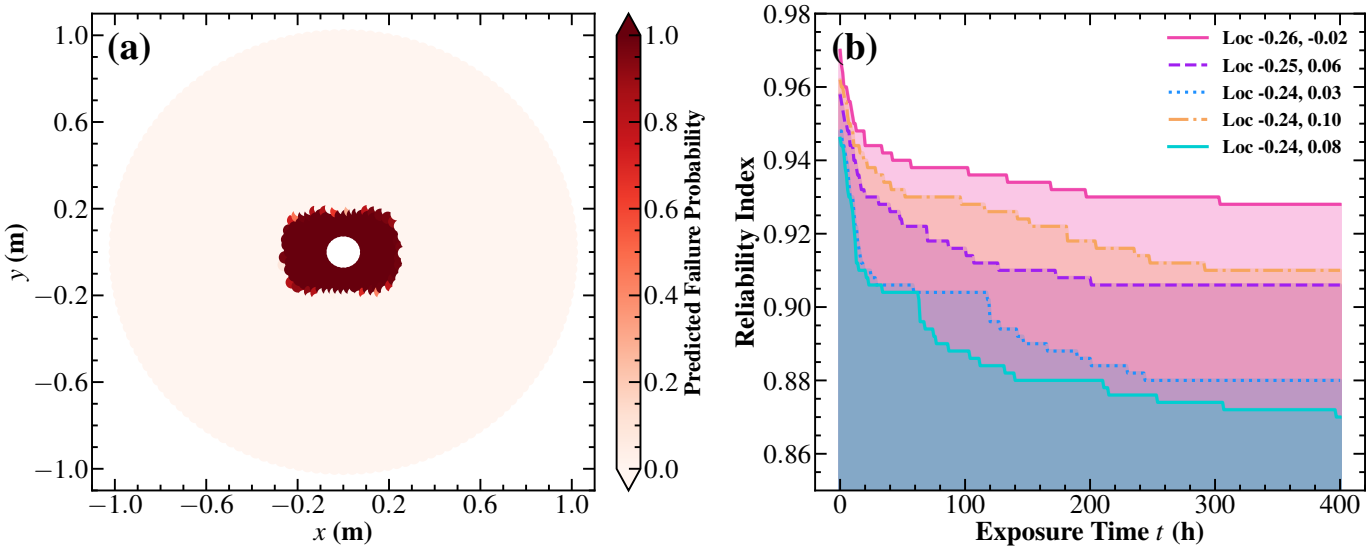


Figure 16: Spatial distribution of instability probability and reliability decay characteristics of typical high-risk points for the open-hole section at 528 m depth, predicted by the HBPINN model.

5.1. Formation Strength Tests

Since wellbore stability depends strongly on the mechanical properties of the rock, uniaxial and triaxial compression tests were conducted on rock samples from the 809–910 m interval. These tests yielded key mechanical parameters, including uniaxial compressive strength, elastic modulus, Poisson's ratio, cohesion, and internal friction angle. A complete formation strength parameter profile was constructed from this data to provide high-fidelity geomechanical inputs for the HBPINN model. The test apparatus and rock samples are shown in Fig. 17.

Sample preparation strictly followed the ASTM D7012-14 standards Perbawa et al. (2021). A diamond hollow drill bit was used to sub-core the pristine core, obtaining standard cylindrical samples with a diameter of 25.4 ± 0.5 mm and a length-to-diameter ratio of 2:1 (height 50.8 ± 0.5 mm). This ensures the elimination of stress concentration effects caused by end constraints. End faces were precision-machined with a double-sided grinder, achieving parallelism within ±0.02 mm and a surface roughness less than 3.2 μm. To reduce the risk of microcrack propagation, samples were prepared and machined in a constant temperature environment (20 ± 1 °C). A low-viscosity kerosene with a kinematic viscosity of less than 4.1 mm²/s was used as the cooling medium. Through X-ray computed tomography (CT) scanning, the finally selected samples were verified to have initial porosity fluctuations within 0.5% and an anisotropy index below 1.1, meeting the requirements for homogeneous specimens Cnudde and Boone (2013).

Triaxial compression tests were performed using a high-temperature, high-pressure system equipped with a multifunctional confining pressure cell. The cell, made of integrally forged maraging steel, is capable of long-term operation under 200 MPa and 200 °C. The confining pressure system used electro-hydraulic servo closed-loop control, achieving a pressure regulation accuracy of 0.1 MPa with a plunger-type intensifier; the system stiffness reached 8×10^9 N/m. Axial loading was accomplished by a 1000 kN servo-actuator with a displacement resolution better than 0.1 μm and a continuously adjustable strain rate (10^{-5}–10^{-2} s^{-1}). The temperature control system integrated annular ceramic heating elements and a liquid nitrogen cooling circuit, with a temperature uniformity better than ±1 °C. The experimental procedure followed the recommended methods of the International Society for Rock Mechanics (ISRM) Ulusay (2015). A 50 μm Polytetrafluoroethylene (PTFE) film was applied to the sample ends to reduce frictional effects Wightman et al. (2025). Confining pressure was applied in a stepwise manner at 0.5 MPa/s. The target confining pressure was held for 30 min, with real-time monitoring of pore pressure to ensure the sample was fully consolidated. Axial loading was conducted in a strain-controlled mode at a rate of 10^{-5} s^{-1}, with axial and radial strains recorded synchronously at a high frequency (100 Hz) to capture post-peak softening and the failure process. The test was terminated when the principal stress difference dropped to 80% of the peak strength to avoid catastrophic failure of the sample.

Data processing was based on continuum mechanics theory. The elastic modulus was determined by a least-squares fit of the linear segment of the stress–strain curve, and the Poisson's ratio was derived from the ratio of axial to radial strain. The strength parameters were inverted using the Drucker–Prager criterion. The ultimate Mohr circle envelope was constructed based on the peak strengths from three tests under different confining pressures. The cohesion and internal friction angle were then inverted using the Levenberg–Marquardt nonlinear least-squares algorithm Gavin (2019). This ensured that the obtained mechanical parameters met the modeling requirements for the subsequent coupled response of the open-hole section. Additionally, data from adjacent wells in the block were incorporated to supplement thermal-hydraulic-chemical related parameters, such as permeability, thermal conductivity, specific heat, and the hydration diffusion coefficient.

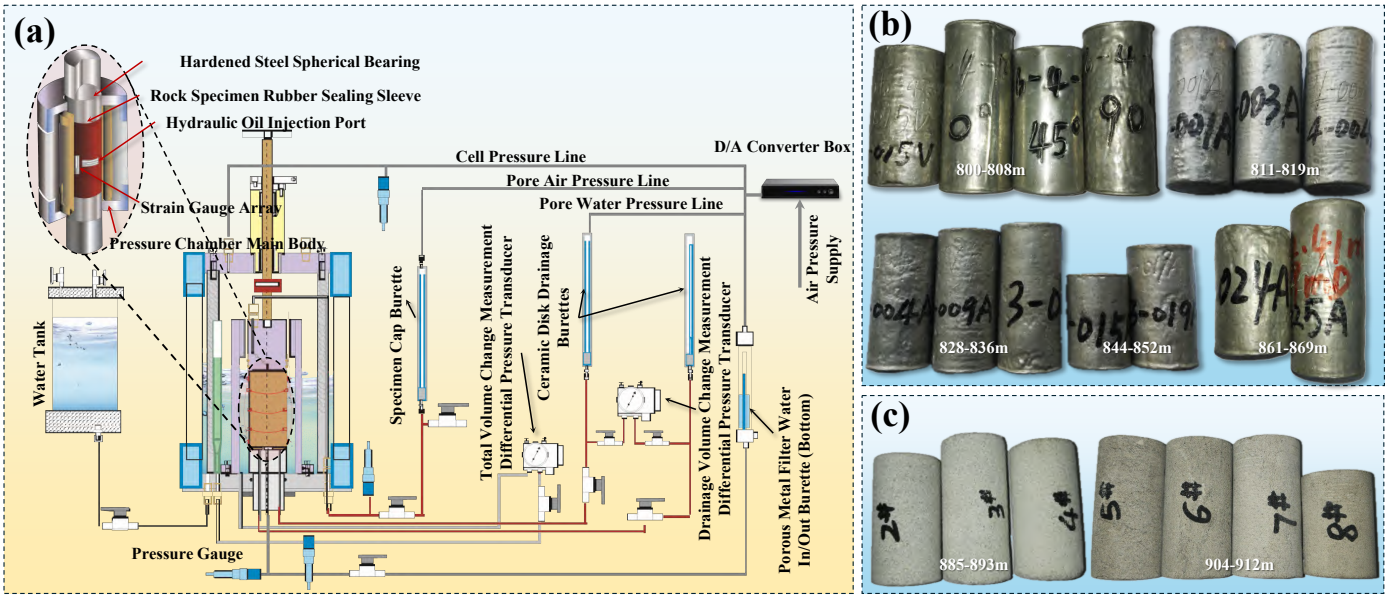


Figure 17: Uniaxial/triaxial compression test apparatus with jacketed and unjacketed rock samples.

5.2. *Prediction of Open-Hole Failure Time*

Fig. 18 presents the lithology profile, key geomechanical parameters, and the earliest failure time evolution profile for the 809–910 m open-hole section of the well in the Caofeidian block, as inferred from the HBPINN model.

This well section is dominated by mudstone and interbedded mudstone–sandstone, with mudstone accounting for 63.7%, indicating clear lithological zonation. The interbedded mudstone–fine sandstone sections have slightly better overall strength and stiffness, with mean uniaxial compressive strength and elastic modulus of 8.93 and 6021.68 MPa, respectively. Their average earliest failure time reaches 135.58 h. In contrast, the mudstone sections are relatively weaker, with a mean strength of 8.65 MPa and an elastic modulus of approximately 5705.78 MPa, corresponding to an average earliest failure time of 131.60 h. The vertical trend analysis shows that the earliest failure time exhibits multi-peak fluctuations with depth. Significant troughs are concentrated within the mudstone layers, which possess weaker mechanical properties and looser pore structures, such as at depths of 833 and 852 m. Here, the shortest tolerable open-hole exposure times drop to 100 and 101 h, respectively. Such locations are more susceptible to triggering instability mechanisms driven by coupled hydration, thermal, and pore pressure disturbances. In contrast, the formation strength in the 895–898 m depth interval is significantly higher, with failure times exceeding 180 h. This trend indicates the positive effect of local structural reinforcement on wellbore stability.

Overall, even within the same lithological unit, the earliest failure time displays nonlinear fluctuations with depth. This highlights the profound vertical heterogeneity of formation parameters along the well depth, as well as the sensitive response of coupled physical fields to subtle parameter changes. Collectively, these factors play a significant regulatory role in wellbore stability. This profile provides quantitative support for determining the time window for running the production casing. Therefore, it improves both the timeliness and engineering safety margin of the third phase well design.

6. Conclusion

This study addressed the stability evolution of open-hole wellbores under the coupled effects of multiphysics fields during long-term exposure. A high-fidelity numerical simulation model was constructed and an HBPINN framework was developed. Through physics-constrained learning and Bayesian inference, this work achieves a joint modeling approach for both state variable prediction and formation parameter uncertainty quantification. The main conclusions are as follows:

1. A coupled multiphysics model for rock state evolution around an open-hole wellbore was constructed. Simulation results show that under continuous drilling fluid invasion, the diffusion characteristics of the pore pressure and temperature fields are highly consistent with Biot–Darcy and porous media heat transfer theories. In contrast, the water-content diffusion process exhibits significant local lag and spatial confinement.
2. An HBPINN architecture was proposed that accurately predicts the multiphysics evolution. The network maintained Von Mises stress prediction errors below 2 MPa for most of the 400-h period and demonstrated superior spatio-temporal generalization, maintaining a high positive R^2 score in extrapolation tests where traditional networks failed completely. This highlights its high physical consistency and reliability even with sparse labeled data.
3. A two-stage Bayesian module successfully quantified instability risk. For a representative case, the analysis revealed a safe exposure time window between 12.53 h and 334.72 h. It also identified asynchronous failure in local high-risk zones, with predicted earliest failure times as low

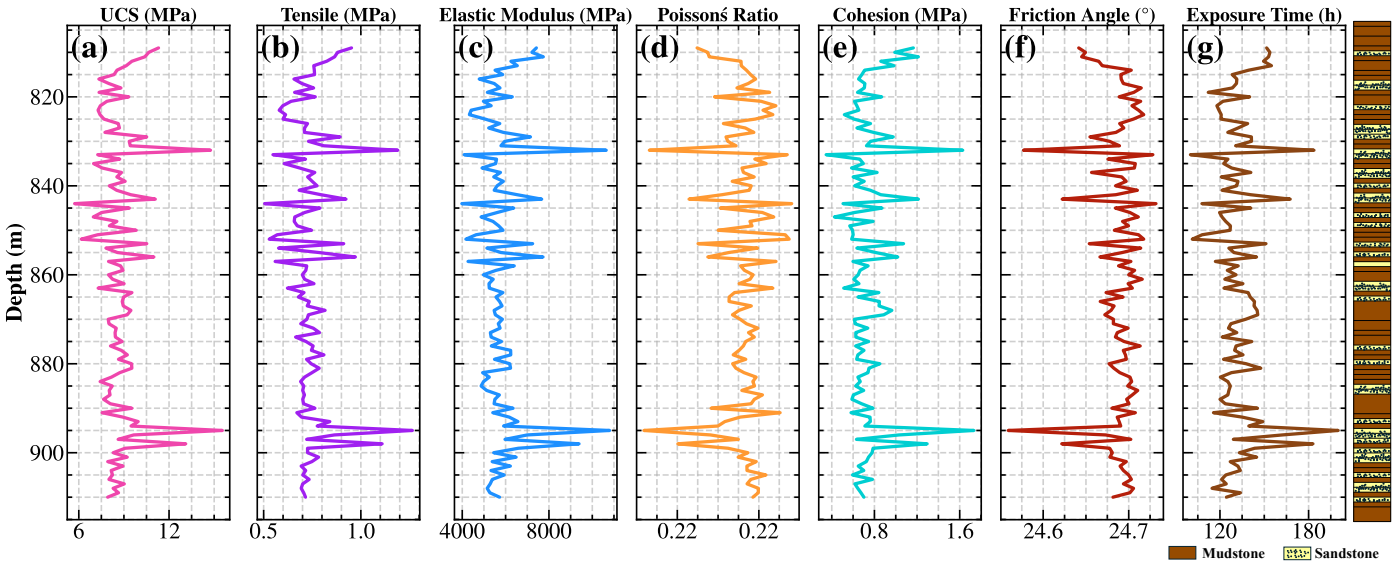


Figure 18: Lithology, key mechanical parameter profiles, and the earliest failure time profile for the 809–910 m open-hole section.

as 100 h in weaker mudstone layers, validating dynamic, spatio-temporal coupled risk warning.

The proposed hybrid framework fuses multiphysics PINNs with Bayesian inference, providing a tool for wellbore stability assessment. The methodology also shows promise for generalization to other subsurface engineering problems, such as hydraulic fracturing and CO_2 sequestration. However, this study has limitations, including simplified physical assumptions like neglecting the dynamic mud cake effect. Future work will focus on integrating more complex mechanisms like anisotropy directly into the PINN loss function and extending the current 2D model to 3D to address more complex engineering scenarios.

References

Alejano, L.R., Bobet, A., 2014. Drucker–prager criterion, in: The ISRM Suggested Methods for Rock Characterization, Testing and Monitoring: 2007-2014. Springer, pp. 247–52.

Baydin, A.G., Pearlmutter, B.A., Radul, A.A., Siskind, J.M., 2018. Automatic differentiation in machine learning: a survey. Journal of Machine Learning Research 18, 1–43.

Biot, M.A., 1941. General theory of three-dimensional consolidation. Journal of Applied Physics 12, 155–64.

Chen, F., Gao, J., Feng, Y., Lin, H., Zhang, B., Bian, G., et al., 2024. Optimizing the wellbore trajectory of directional wells considering wellbore stability Subjected to the non-independence and uncertainty of geomechanical parameters. Geoenergy Science and Engineering 241, 213085.

Cnudde, V., Boone, M.N., 2013. High-resolution X-ray computed tomography in geosciences: A review of the current technology and applications. Earth-Science Reviews 123, 1–17.

Coussy, O., 2004. Poromechanics. John Wiley & Sons.

Ding, Y., Liu, X., Liang, L., Xiong, J., Li, W., Wei, X., et al., 2023. Wellbore stability model in shale formation under the synergistic effect of stress unloading-hydration. Petroleum Exploration and Development 50, 1478–86.

Dongo, D.F., Relvas, S., 2025. Evaluating the role of the oil and gas industry in energy transition in oil-producing countries: A systematic literature review. Energy Research & Social Science 120, 103905.

Drucker, D.C., Prager, W., 1952. Soil mechanics and plastic analysis or limit design. Quarterly of Applied Mathematics 10, 157–65.

Fan, Y., Pang, H., Jin, Y., Meng, H., Lu, Y., Wei, S., et al., 2025. Integration of image recognition and expert system for real-time wellbore stability analysis. Advances in Geo-Energy Research 15, 158–71.

Feng, Y., Li, X., Gray, K.E., 2018. An easy-to-implement numerical method for quantifying time-dependent mudcake effects on near-wellbore stresses. Journal of Petroleum Science and Engineering 164, 501–14.

Gavin, H.P., 2019. The Levenberg-Marquardt algorithm for nonlinear least squares curve-fitting problems. Technical Report. Department of Civil and Environmental Engineering, Duke University. August.

Gelman, A., Carlin, J.B., Stern, H.S., Rubin, D.B., 1995. Bayesian Data Analysis. Chapman and Hall/CRC.

Goodfellow, I., Bengio, Y., Courville, A., Bengio, Y., 2016. Deep Learning. MIT press Cambridge.

He, Y., Zio, E., Yang, Z., Xiang, Q., Fan, L., He, Q., et al., 2025. A systematic resilience assessment framework for multi-state systems based on physics-informed neural network. Reliability Engineering & System Safety 257, 110866.

Hendrycks, D., Gimpel, K., 2016. Gaussian error linear units (GELUs). arXiv preprint arXiv:1606.08415 .

Hoffman, M.D., Gelman, A., 2014. The No-U-Turn sampler: adaptively setting path lengths in Hamiltonian Monte Carlo. Journal of Machine Learning Research 15, 1593–623.

Huang, T., Pu, X., Luo, X., Yu, H., Xu, S., 2014. Wellbore stability analysis of shale formations based on fluid-solid coupling theory. Journal of Oil and Gas Technology 36, 117–21.

Institute, AP, 2017. API RP 13B-1 Recommended Practice for Field Testing Water-based Drilling Fluids. Technical Report. American Petroleum Institute. (5th ed).

Jerez, D.J., Chwała, M., Jensen, H.A., Beer, M., 2024. Optimal borehole placement for the design of rectangular shallow foundation systems under undrained soil conditions: A stochastic framework. Reliability Engineering & System Safety 242, 109771.

Kamgue Lenwoue, A.R., Li, Z., Tang, C., Zhang, W., Ding, S., Hu, P., et al., 2023. Recent advances and challenges of the application of artificial intelligence to predict wellbore instabilities during drilling operations. SPE Drilling & Completion 38, 645–62.

Krygier, N., Solarin, A., Orozova-Bekkevold, I., 2020. A drilling company's perspective on non-productive time NPT due to well stability issues, in: SPE Norway Subsurface Conference, SPE. p. D011S04R02.

Li, J.Y., Tang, J.Z., Zhao, X.Z., Fan, B., Jiang, W.Y., Song, S.Y., et al., 2025. A large-scale, high-quality dataset for lithology identification: Construction and applications. Petroleum Science .

Liu, Z., Ma, Q., Cai, B., Shi, X., Zheng, C., Liu, Y., 2022. Risk coupling analysis of subsea blowout accidents based on dynamic Bayesian network and NK model. Reliability Engineering & System Safety 218, 108160.

Lohr, S.L., 2021. Sampling: Design and Analysis. Chapman and Hall/CRC.

Loshchilov, I., Hutter, F., 2017a. Decoupled weight decay regularization. arXiv preprint arXiv:1711.05101 .

Loshchilov, I., Hutter, F., 2017b. SGDR: Stochastic gradient descent with warm restarts, in: International Conference on Learning Representations.

Lubliner, J., 2008. Plasticity Theory. Courier Corporation.

Ma, T., Liu, J., Fu, J., Qiu, Y., Fan, X., Martyushev, D.A., 2025. Fully coupled thermo-hydro-mechanical model for wellbore stability analysis in deep gas-bearing unsaturated formations based on thermodynamics. Rock Mechanics and Rock Engineering 58, 33–64.

McKay, M.D., Beckman, R.J., Conover, W.J., 2000. A comparison of three methods for selecting values of input variables in the analysis of output from a computer code. Technometrics 42, 55–61.

Nield, D.A., Bejan, A., 2006. Convection in Porous Media. Springer.

Perbawa, A., Gramajo, E., Finkbeiner, T., Santamarina, J., 2021. Rock triaxial tests: global deformation vs local strain measurements—implications. Rock Mechanics and Rock Engineering 54, 3527–40.

Pirhadi, A., Kianoush, P., Ebrahimabadi, A., Shirinabadi, R., 2023. Wellbore stability in a depleted reservoir by finite element analysis of coupled thermo-poro-elastic units in an oilfield, SW Iran. Results in Earth Sciences 1, 100005.

Rafieepour, S., Zamiran, S., Ostadhassan, M., 2020. A cost-effective chemo-thermo-poroelastic wellbore stability model for mud weight design during drilling through shale formations. Journal of Rock Mechanics and Geotechnical Engineering 12, 768–79.

Raissi, M., Perdikaris, P., Karniadakis, G.E., 2019. Physics-informed neural networks: A deep learning framework for solving forward and inverse problems involving nonlinear partial differential equations. Journal of Computational Physics 378, 686–707.

Saber, E., Qu, Q., Aminossadati, S.M., Zhu, Y., Chen, Z., 2024. Horizontal borehole azimuth optimization for enhanced stability and coal seam gas production. Rock Mechanics Bulletin 3, 100100.

Siddiqui, M.A.Q., Regenauer-Lieb, K., Roshan, H., 2024. Thermo-Hydro-Chemo-Mechanical (THCM) continuum modeling of subsurface rocks: A focus on thermodynamics-based constitutive models. Applied Mechanics Reviews 76, 031001.

Song, C., Xiao, R., Zhang, C., Zhao, X., Sun, B., 2024. Simulation-free reliability analysis with importance sampling-based adaptive training physics-informed neural networks: Method and application to chloride penetration. Reliability Engineering & System Safety 246, 110083.

Song, Z., Song, Y., Yang, J., Liu, B., Gao, B., Tang, J., 2025. A multi-objective reinforcement learning framework for real-time drilling optimization based on symbolic regression and perception. Geoenergy Science and Engineering 244, 213392.

Srivastava, N., Hinton, G., Krizhevsky, A., Sutskever, I., Salakhutdinov, R., 2014. Dropout: a simple way to prevent neural networks from overfitting. The Journal of Machine Learning Research 15, 1929–58.

Sunnåker, M., Busetto, A.G., Numminen, E., Corander, J., Foll, M., Dessimoz, C., 2013. Approximate Bayesian computation. PLOS Computational Biology 9, e1002803.

Udegbunam, J.E., Aadnøy, B.S., Fjelde, K.K., 2014. Uncertainty evaluation of wellbore stability model predictions. Journal of Petroleum Science and Engineering 124, 254–63.

Ulusay, R., 2015. The ISRM suggested methods for rock characterization, testing and monitoring: 2007-2014. Springer.

Wang, H., Li, B., Lei, L., Xuan, F., 2024. Uncertainty-aware fatigue-life prediction of additively manufactured Hastelloy X superalloy using a physics-informed probabilistic neural network. Reliability Engineering & System Safety 243, 109852.

Wightman, A., Dickinson, S., Jeong, C.G., Shanmugarajah, T., Billings, M., 2025. Importance of sample height–diameter ratio in triaxial testing with free ends for determination of the critical state of sands. Geotechnical Testing Journal 48, 147–65.

Wu, J., Liu, W., Li, J., Han, B., Tan, Q., Lin, H., et al., 2024a. Artificial neural network prediction of wellbore stability in offshore shallow formations. Geoenergy Science and Engineering 243, 213322.

Wu, S., Hu, Y., Zhang, L., Liu, S., Xie, R., Yin, Z., 2024b. Intelligent risk identification for drilling lost circulation incidents using data-driven machine learning. Reliability Engineering & System Safety 252, 110407.

Wu, S., Zhang, Q., Li, B., Zhang, L., Zheng, W., Li, Z., et al., 2023. Reliability analysis of subsea wellhead system subject to fatigue and degradation during service life. Reliability Engineering & System Safety 239, 109494.

Zhang, Z., Tang, J., Fan, B., Zhao, X., Jin, F., Chen, C., et al., 2024a. An intelligent lithology recognition system for continental shale by using digital coring images and convolutional neural networks. Geoenergy Science and Engineering 239, 212909.

Zhang, Z., Tang, J., Zhang, J., Meng, S., Li, J., 2024b. Modeling of scale-dependent perforation geometrical fracture growth in naturally layered media. Engineering Geology 336, 107499.

Zhou, Y., 2023. Worldwide carbon neutrality transition? Energy efficiency, renewable, carbon trading and advanced energy policies. Energy Reviews 2, 100026.

Table 3: HBPINN Algorithm Flow.

Input:
X: Set of collocation points in the physical and temporal domain
Y: Limited supervisory label data (e.g., from COMSOL Multiphysics)
$p(\theta)$: Prior distribution for the set of physical parameters to be inferred, $\theta = \{E_0, c_0, \phi_0, w_0\}$
$\Theta_{NN}^{(0)}$: Initial parameters (weights and biases) for the neural network
Output:
Θ_{NN}: Converged neural network parameters
$p(\theta \mid D)$: Posterior distribution of the physical parameters θ
$P_f(t, x, y), R(t, x, y), t_{\text{safe}}(x, y)$: Spatio-temporal failure probability field, reliability field, and safe time window
function HBPINN
    Initialize: Initialize the neural network $N(t, x, y; \Theta_{NN})$ with parameters $\Theta_{NN}^{(0)}$
    Construct Loss Function: $L_{\text{total}} = \omega_p L_p + \omega_{wT} L_{wT} + \omega_y L_y + \omega_{\text{data}} L_{\text{data}} + \omega_{BC} L_{BC} + \omega_{IC} L_{IC}$
    Set Learning Rate Scheduler: Set up the three-stage cosine annealing with restarts policy η_t
    for epoch = 1 to 10^5 **do**
        Sample a batch of collocation points from X
        Compute the physics residual losses L_p, L_{wT}, L_y and the boundary/initial condition losses L_{BC}, L_{IC}
        if Y is available **then**
            compute the data fitting loss L_{data}
        end if
        Compute the weighted sum to get L_{total}
        Update network parameters using the AdamW optimizer: $\Theta_{NN} \leftarrow \Theta_{NN} - \eta_t \cdot \nabla_{\Theta_{NN}} L_{\text{total}}$
        Check the Early Stopping criterion; terminate training if met
    end for
    Freeze Network: Fix the converged neural network parameters Θ_{NN}
    Construct Likelihood Function: Build the approximate likelihood function $L(\theta)$ based on the physics yield function residual F
    Posterior Sampling: Use NUTS to sample from the posterior distribution $p(\theta \mid D) \propto L(\theta) \cdot p(\theta)$ to obtain the set of posterior parameter samples $\theta^{(i)}$
    Post-processing and Risk Quantification:
    for each spatio-temporal point (t, x, y) to be evaluated **do**
        for each posterior parameter sample $\theta^{(i)}$ from 1 to N_{samples} **do**
            a. Compute $\sigma_y^{(i)}$ and $\varepsilon_y^{(i)}$ based on $\theta^{(i)}$
            b. Predict $\sigma_{\text{eq}}^{(i)}$ and $\varepsilon_p^{(i)}$ from the neural network using $\theta^{(i)}$ and the fixed Θ_{NN}
            c. Compute $P_{\text{inst}}(\theta^{(i)}) = 0.4 \cdot L(\sigma_{\text{eq}}^{(i)}/\sigma_y^{(i)}) + 0.6 \cdot L(\varepsilon_p^{(i)}/\varepsilon_y^{(i)})$
        end for
        Calculate Final Failure Probability $P_f(t, x, y)$
    end for
    Calculate Higher-Order Metrics: Compute $R(t, x, y) = 1 - P_f(t, x, y)$ and $t_{\text{safe}}(x, y)$ based on P_f
    return $\Theta_{NN}, p(\theta \mid D), P_f(t, x, y), R(t, x, y), t_{\text{safe}}(x, y)$
end function